Journal of Catalysis xxx (xxxx) xxx

Contents lists available at ScienceDirect

Journal of Catalysis

journal homepage: www.elsevier.com/locate/jcat

Al_2O_3 nanofibers prepared from aluminum Di(*sec*-butoxide)acetoacetic ester chelate exhibits high surface area and acidity

M.A. Rodriguez-Olguin [a], H. Atia [b], M. Bosco [c,d], A. Aguirre [c], R. Eckelt [b], E.D. Asuquo [e], M. Vandichel [f,*], J.G.E. Gardeniers [a,*], A. Susarrey-Arce [a,*]

[a] Mesoscale Chemical Systems, MESA+ Institute, University of Twente, PO. Box 217, 7500AE Enschede, the Netherlands
[b] Leibniz Institute for Catalysis, Albert-Einstein-Straße 29a, D-18059 Rostock, Germany
[c] Instituto de Desarrollo Tecnológico para la Industria Química (INTEC), Universidad Nacional del Litoral, CONICET, Güemes 3450, S3000GLN Santa Fe, Argentina
[d] Facultad de Ingeniería Química, Universidad Nacional del Litoral (UNL), Santiago del Estero 2829, Santa Fe 3000, Argentina
[e] National Graphene Institute, Department of Materials, University of Manchester, Oxford Road, Manchester M13 9PL, United Kingdom
[f] Department of Chemical Sciences and Bernal Institute, University of Limerick, Limerick V94 T9PX, Republic of Ireland

ARTICLE INFO

Article history:
Received 13 August 2021
Revised 22 October 2021
Accepted 16 November 2021
Available online xxxx

Keywords:
Acidity
Electrospinning
Nanofibers
NH_3-TPD
Porous Alumina
DFT

ABSTRACT

Alumina (Al_2O_3) is a widely used material for catalysis in the chemical industry. Besides a high specific surface area, acid sites on Al_2O_3 play a crucial role in the chemical transformation of adsorbed molecules, which ultimately react and desorb from the catalyst. This study introduces a synthetic method based on electrospinning to produce Al_2O_3 nanofibers (ANFs) with acidity and porosity tuned using different aluminum precursor formulations. After electrospinning and heat treatment, the nanofibers form a non-woven network with macropores (~4 μm). Nanofibers produced from aluminum di(*sec*-butoxide) acetoacetic ester chelate (ASB) show the highest total acidity of ca. 0.70 μmol/m^2 determined with temperature-programmed desorption of ammonia (NH_3-TPD) and BET. The nature of the acid site in ASB ANFs is studied in detail with infrared (IR) spectroscopy. Pyridine is used as a molecular probe for the identification of acid sites in ASB. Pyridine showed the presence of Lewis acid sites prominently. Density-functional theory (DFT) is conducted to understand the desorption kinetics of the adsorbed chemical species, such as ammonia (NH_3) on crystalline γ-Al_2O_3. For our analysis, we focused on a mobile approach for chemisorbed and physisorbed NH_3. The computational results are compared with NH_3-TPD experiments, ultimately utilized to estimate the desorption energy and kinetic desorption parameters. The experiments are found to pair up with our simulation results. We predict that these non-woven structures will find application as a dispersion medium of metallic particles in catalysis.

1. Introduction

Al_2O_3 is one of the most important acid catalysts applied in biomass conversion to produce chemicals and fuels [1–6]. The material also functions as a dispersion medium (i.e., support) for alkali metals, halogens, noble metals, and metal oxides in the petroleum and automotive sector [7–13]. Various polymorphs α-, γ-, η-, θ-, δ-, κ-, and χ- of Al_2O_3 can be found in literature [14,15]. This wide range of Al_2O_3 has unique properties, such as acidity, high specific surface area, and excellent chemical and thermal stability [4,13,16–20]. Among these properties, a key characteristic in Al_2O_3 is the acid site [21,22,23]. Favorable combinations of acid sites, such as Brønsted acid sites (BAS) and Lewis acid sites (LAS), can be achieved by changing the Al precursor or the addition of other additives during Al_2O_3 synthesis [24–27]. Another key parameter is the pore size distribution. Al_2O_3 can contain different types of porosity, where the micropores, with a pore width distribution lower than 2 nm, contain the active sites for (selective) reaction, and mesopores, with a pore width distribution in the range of 2 to 50 nm, are the diffusion pathways [4,28,29]. Ultramicropores and supramicropores with a pore size between 0.7 and 2 nm,[30] are not discussed here but are known to contribute to the total surface area.

Synthetic approaches for the production of Al_2O_3 and its properties have been extensively studied over the years [4,31–55]. Typical methods to structure Al_2O_3 are extrusion[13], anodization[56], injection molding,[57] and 3D-printing [57,58]. Current developments are focused on geometrical optimization to control reaction

* Corresponding authors.
E-mail addresses: matthias.vandichel@ul.ie (M. Vandichel), j.g.e.gardeniers@utwente.nl (J.G.E. Gardeniers), a.susarreyarce@utwente.nl (A. Susarrey-Arce).

https://doi.org/10.1016/j.jcat.2021.11.019
0021-9517/

rates via mass transfer and diffusivity but often do not pay much attention to the chemical properties of structured Al_2O_3. A way to introduce hierarchy in Al_2O_3 catalysts is by shaping the material in the form of a non-woven nanofiber network. The general idea is that the fiber network will generate macropores that facilitate reactant and product diffusion, whereas the intrinsic porosity in ANFs will provide efficient surface area for reaction kinetics [59,60]. Many applications for non-woven nanofibers have already been promoted, e.g., in environmental science, energy storage, and energy conversion [28,61–65]. However, applications of ANFs in catalysis are still limited (**Table S1** and **Table S2**), possibly due to the difficulty of obtaining ANFs with both high surface area and acidity comparable to known commercial catalysts.

A convenient method for the production of non-woven nanofiber networks is electrospinning [28,64,66–83]. A drawback of this method, compared to many other 3D printing methods, is that electrospinning generally lacks the control to make ordered spaces between intertwining nanofibers. Advancements in the field of electrospinning have demonstrated the possibility of aligning nanofibers (e.g., melting electrospinning),[86] but the method is still limited to polymers and biomaterials [84]. Nevertheless, the electrospinning technique provides excellent precursor versatility, which can be tuned to obtain various functionalities (Table S1). For example, it has been recognized that the role of chelating agents [85], such as ASB, is crucial for mesopore formation [23,86–88]. An accepted mechanism for ASB-chelate is a condensation reaction. During this reaction, unreacted species (such as OH ligands and other small molecules) can promote the formation of mesopores [86]. An additional contribution to the pore size and pore type is the polymer template of the electrospun fibers [69]. In this case, the template can be removed by applying a heat treatment and form pores and other asperities over the Al_2O_3. It should be noted that heat treatment can also alter the physical and chemical properties of Al_2O_3 nanofibers. This includes the formation of amorphous, semicrystalline, and crystalline Al_2O_3 [14,15].

In this report, we studied different Al-formulations (e.g., ASB-chelate, aluminum nitrate, alumina nanoparticles used as additives, and combinations) as a first step towards the structural design of ANF networks for catalysis. Among the produced ANFs, ASB reveals the highest acidity as determined with NH_3-TPD. The γ-Al_2O_3 nanofibers obtained from ASB are compared with two commercial γ-Al_2O_3 controls, i.e., amorphous and semicrystalline ANFs from ASB. γ-Al_2O_3 nanofibers from ASB show similar acidity, if not even better than the commercial counterpart. IR spectroscopy of pyridine is used to identify the type of acid sites present in the ASB ANFs. Density-functional theory (DFT) has been conducted to understand the desorption kinetics of the adsorbed chemical species, such as ammonia (NH_3) on γ-Al_2O_3. Conclusions are drawn regarding NH_3 reaction kinetics and surface desorption mechanisms. We expect the use of these types of AFNs as a dispersing medium for metal or metal oxide nanoparticles, which is very much desired in the field of heterogeneous catalysis.

2. Experiments and methods

2.1. Electrospinning of Al_2O_3 nanofibers

ANFs (amorphous, semicrystalline, and crystalline) were prepared using a commercial electrospinning system from IME Technologies (The Netherlands), which was operated utilizing a stainless steel needle of 0.4 mm inner diameter at a separation distance of 12 cm from the aluminum collector plate. $Al(NO_3)_3{\cdot}9H_2O$ (AN) ACS grade and $C_{14}H_{27}AlO_5$ (ASB) technical grade from Alpha Aesar were used to prepare the aluminum stock solutions (Al-stock). Nanoparticulated γ-Al_2O_3 from Sigma-Aldrich (AL) was used as an additive. The following compositions were created using the mentioned precursors and additives: ASB, AN, AN-AL, ASB-AL, AN-ASB, and AN-ASB-AL. All these compositions contained polyvinylpyrrolidone (PVP, MW $\sim$ 1,300,000), N, N-dimethylformamide (DMF), and ethanol. The aluminum precursor concentration was 0.14 M. The final concentrations for PVP and DMF were 8.09 mM and 7.2 M for all cases. Samples with more than one aluminum precursor were mixed, maintaining the same Al molar concentration. A summary of prepared precursors and other electrospinning parameters, like voltages and infusion rates, can be found in **Table S3**. All samples were collected at 298 K and relative humidity of 25%. After fiber deposition, the ANFs were dried in a furnace at 353 K for 12 h to remove the excess solvent. The obtained ANFs (AN, AN-AL, ASB-AL, AN-ASB, AN-ASB-AL) were annealed at 1173 K (1 K/min) for 1 h to obtain γ-Al_2O_3. Fibers from ASB were annealed at 873 K (ASB873K) and 1023 K (ASB1023K) at 1 K/min for 1 h to obtain amorphous and semicrystalline ANFs.

2.2. Morphological characterization

Scanning electron microscopy (SEM) images of samples AN, ASB, AN-ASB, AN-AL, ASB-AL, and AN-ASB-AL were taken using an FEI Quanta 450 SEM microscope at 10 kV coupled with in-lens detectors. High-resolution (HR)-SEM images of samples AN and ASB1173K were taken using a Zeiss MERLIN SEM microscope operated at 0.65 kV coupled with High-Efficiency Secondary Electron Detector (HE-SE2). SEM-scanning transmission electron microscope (STEM) was recorded at 20 kV. Prior to STEM analysis, samples were sonicated in ethanol. Sample sonication led to the breaking of the ANFs.

2.3. Structural characterization

The crystallographic phase of all samples was analyzed by X-ray powder diffraction (D2 PHASER, Bruker) using Cu Kα radiation (λ = 1.5418 Å) operated at 30 kV, 10 mA, in the 2θ range between 15 and 80°, employing a step size of 0.05° and a scan speed of 0.1°/s. A Si low background sample holder (Bruker) was used for all samples.

2.4. Chemical surface characterization

X-ray photoelectron spectroscopy (XPS) general survey analysis was performed in a Quantera SXM machine from Physical Electronics using monochromated Al Kα (1486.6 eV). The ANFs powder samples were fixed on double-sided adhesive carbon tape mounted on a stainless-steel holder. Low energy electron flood gun was used to supply the missing photo- and Auger electrons. The electron binding energies were referenced to aliphatic carbon C 1 s at 284.8 eV. The obtained peaks analysis was made using the PHI Multipak V9.9.0.8 software (Physical Electronics, Inc.).

2.5. Pore property and textural characterization

BET surface area, pore-volume, and pore diameter of the ANF samples were determined from the nitrogen adsorption/desorption isotherms at 77 K on a Micrometrics ASAP 2010 instrument. Before the measurement, each sample was evacuated at 473 K for 4 h. The pore size distributions were calculated from the desorption branch of the isotherm using the Barrett-Joyner-Halenda (BJH) method [29]. Commercial AL and γ-Al_2O_3 PLURALOX SCFa-140 (ALS) from Sasol were used as control during BET measurements.

2.6. Mercury intrusion porosimetry

Mesoporous diameter was determined by mercury intrusion porosimetry on a Poremaster PM-33–14 (Quantachrome®) equipment. The pore diameter distribution was calculated using Washburn's equation[89,90]:

$$D_v(r) = \frac{dV_{Hg}}{dP}\left[\frac{P^2}{2\gamma Cos\theta}\right]$$

V_{Hg} stands for the volume of mercury intruded, γ is the fluid surface tension, θ is the fluid contact angle, and dP is pressured across the interface.

2.7. Acid sites characterization by pyridine adsorption

The nature and strength of LAS and BAS were determined through the adsorption andtemperature-programmed desorption of pyridine (called Py hereafter) over the ANFs and commercial AL and ALS. The ANFs were analyzed with IR spectroscopy through in situ transmission on self-supported wafers (4–10 mg, 13 mm of diameter) pressed at 5 t cm^{-2} (490 MPa). The wafers were placed into a Pyrex IR cell fitted with water-cooled NaCl windows. More details of the experimental setup can be found elsewere[91]. Before the adsorption experiments, each sample was pretreated in situ at 723 K (10 K/min) for 30 min under He flow (50 sccm), then cooled down to 303 K, and the reference IR spectra of the "clean wafer" was taken. The samples were exposed to a flow of He containing evaporated Py. The physisorbed Py was further removed under flowing He until the spectra of the adsorbed Py remain stable (about 60 min). The thermal programed desorption of Py (TPD) was measured from 303 K to 723 K at 5 K/min in a flow of He (50 ml/min).

The spectra were acquired with a Nicolet Magna 550 FTIR spectrometer with a cryogenic MCT detector (4 cm^{-1} resolution, 25 scans). The gas used in this study was high purity grade He (INDURA UHP 99.999%) and was further purified through a molecular sieve (3 Å), and MnO/Al_2O_3 traps to remove water and oxygen impurities, respectively.

2.8. NH_3-TPD

NH_3-TPD experiments were performed using a Micromeritics Autochem II 2910 instrument to measure the sample's total acidity. Prior to NH_3 adsorption, 150 mg of the sample was loaded into a U-shaped quartz reactor and heated from RT to 673 K with 10 K/min in a flow of He (50 ml/min), held for 30 min at 673 K (to remove any adsorbed species on the surface). After that, the reactor was cooled to 373 K. The sample was saturated with 1% NH_3 in He (50 ml/min) for 120 min at 373 K, followed by helium flushing (50 ml/min) for 60 min at 373 K to remove physisorbed NH_3. The sample was then heated to 1073 K at a rate of 10 K/min in He flowed (50 ml/min) and held at 1073 K for 30 min for NH_3 desorption. Analysis of the effluent gases was performed with a Quadrupole mass spectrometer (Balzers Omnistar) using m/z = 15. Commercial AL and γ-Al_2O_3 PLURALOX SCFa-140 (ALS) from Sasol were used as references for comparison.

2.9. Computational methods

NH_3 adsorption was studied using periodic DFT-D (Dispersion-corrected Density Functional Theory) calculations with the Vienna Ab Initio Simulation Package (VASP 5.4.4) [92,93]. BEEF-vdW (Bayesian Error Estimation Functional with van der Waals correlation) was employed to also account for van der Waals interactions for all reaction intermediates [94]. The one-electron Kohn-Sham orbitals were expanded on a plane-wave basis with a kinetic energy cut-off of 550 eV for all calculations. Furthermore, the Projector Augmented Wave approximation (PAW) was used [95]. For the Brillouin zone sampling, a 3x3x1 k-point grid was employed and a vacuum of more than 16 Å. Gaussian smearing[92] of 0.1 eV was applied to improve convergence. The geometries were considered converged if the largest force was below 0.03 eV/Å.

Additionally, the convergence criterion for the Self-Consistent electric Field (SCF) problem was set to 10^{-6} eV for structural optimizations. Next, for γ-Al_2O_3, a periodic (1 1 0) surface slab was constructed. The surface is composed of 4 layers of Al_8O_{12} to obtain periodic unit cells terminated with Al-groups with different coordination numbers and surface implantation, shown in **Figure S1**. Similar model systems were previously employed to study γ-Al_2O_3 containing model systems [20,96,97,98]. As presented in **Figure S1**, even chemisorbed water can be removed during a pretreatment at a high temperature above ~ 900 K and relatively low water partial pressures. However, if the pretreatment temperature is lower than ~ 900 K, the γ-Al_2O_3 surface still contains chemisorbed water. Therefore, we have considered a γ-Al_2O_3 [110] system with chemisorbed water for NH_3 adsorption. Furthermore, the computational results for NH_3 adsorption on a γ-Al_2O_3 [110] system without chemisorbed water are presented in the **Supporting Information**.

For the γ-Al_2O_3 model systems, Partial Hessian Vibrational Analysis (PHVA) is employed only for the surface species while keeping the rest of the system stationary. The numerical partial Hessian was calculated by displacements in x, y, and z-directions of ± 0.02 Å, and the vibrational modes were extracted using the normal mode analysis as implemented in the post-processing toolkit TAMKIN [99]. The PHVA was used to obtain zero-point corrections and free energy contributions. The Gibbs free energies of adsorption were calculated at various temperatures. In the immobile adsorbate approach applied to chemisorbed NH_3, a complete loss in translational and rotational entropy of the NH_3 adsorbates upon adsorption or chemisorption on the γ-Al_2O_3 model is considered. However, at higher temperatures, it is expected that the adsorbed NH_3 can translate more freely over the model surface as barriers for hopping between adsorption sites are hardly activated (10–20 kJ/mol). Therefore, a mobile adsorbate approach has been employed for physisorbed NH_3 molecules, maintaining 2 of their translational degrees of freedom. In other words, whenever one of the NH_3 adsorbate molecules was not fully chemisorbed, the molecule was treated as being physisorbed, maintaining a free-translator in two dimensions. Therefore, the additional translational entropy was then calculated by treating the adsorbed NH_3 species as a two-dimensional gas [100,101,102].

3. Results and discussions

3.1. γ-Al_2O_3 in the form of nanofibers

The precursor composition of the γ-Al_2O_3 nanofibers is varied, intending to achieve the highest acidity and highest surface area. The selected precursors ASB, AN, AL, and their combinations (ASB-AL, AN-ASB, and AN-ASB-AL) are shown in **Table S3**. Among the precursors used to produce ANFs, ASB results in the ideal candidate because it can lead to a sol–gel that can be added directly to the precursor for electrospinning [103]. It is important to note that variations in the precursor composition can alter electrospinning conditions (**Table S3**) [63,83,104–106] in some cases leading to nanofiber instabilities. SEM images of the γ-Al_2O_3 nanofibers annealed at 1173 K are presented in Fig. 1. Here, ASB1173K (Fig. 1**(a)**), AN (Fig. 1**(b)**), and their combinations (AN-ASB, Fig. 1**(c)**), including additives (ASB-AL, AN-AL, AN-ASB-AL) in Fig. 1**(d-**

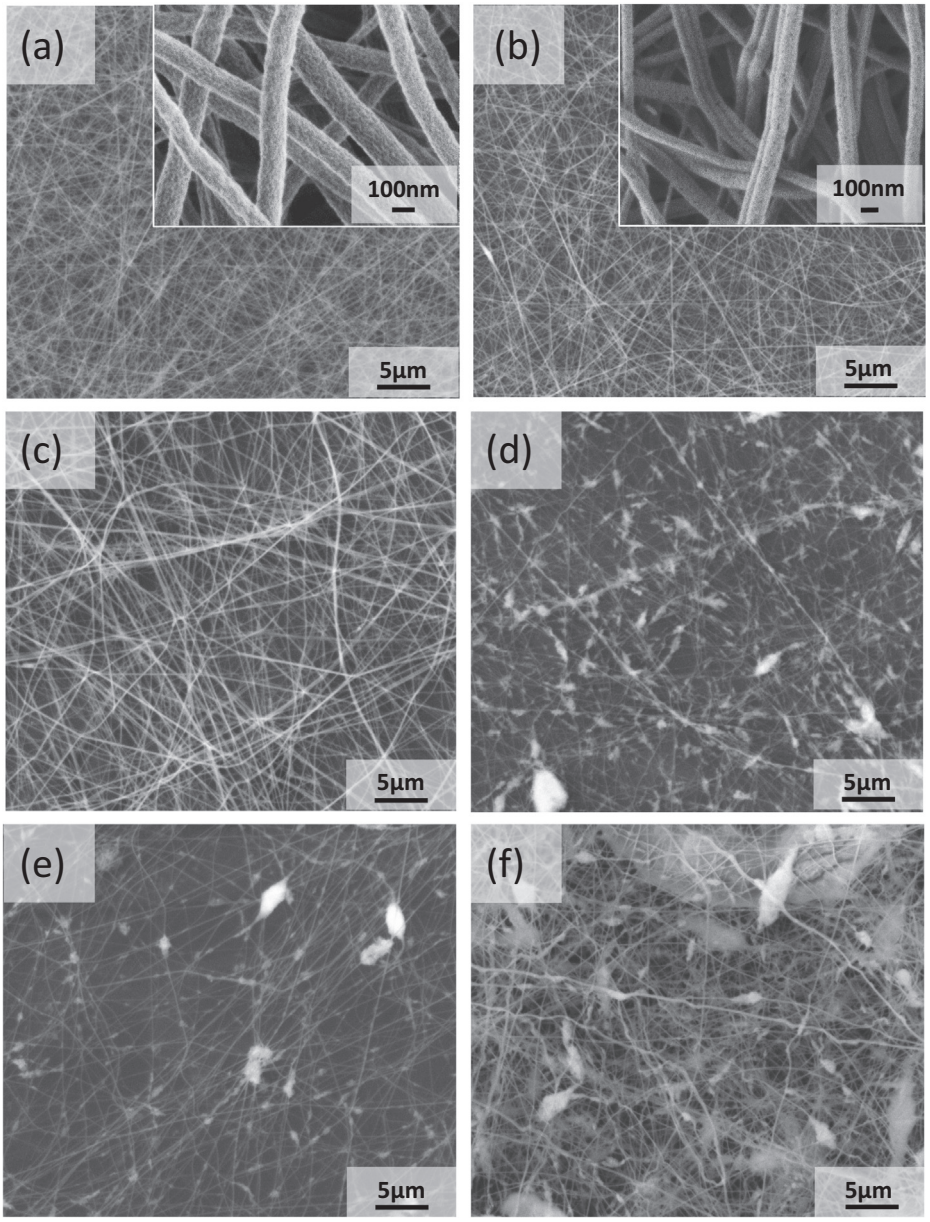

Fig. 1. SEM pictures of (a) ASB1173K, (b) AN, (c)AN-ASB, (d) ASB-AL, (e) AN-AL, and (f)AN-ASB-AL ANFs calcined at 1173 K.

f), reveal a non-woven structure alike with some axisymmetric instabilities. The γ-Al_2O_3 nanofibers with ASB1173K, AN, and AN-ASB have a fibrous structure with nanofiber diameters of 83 ± 11, 85 ± 15, and 112 ± 20 nm. Insets in Fig. 1 **(a-b)** and **Figure S2** visualize the nanofiber roughness observed for most of the ANFs in Fig. 1. The roughness can be attributed to the removed organic content after annealing from ASB and AN. The addition of AL to ASB and AN affects the overall ANF morphology. These ANFs are more inhomogeneous than ASB, AN, and AN-ASB. Some agglomerates are found in Fig. 1 **(d-f)**, which are thought to come from the fiber whipping instability during the fly of fibers towards the collector plate. AN-ASB-AL results in nanofibers of 91 ± 29 nm in diameter. Due to their poor fiber characteristics (Fig. 1 **(d-e)**), ASB-AL and AN-AL have not been further investigated. A STEM image of the commercial AL lacking fibrous morphology[107] is shown in **Figure S3** for comparison. Poor fiber characteristics in Fig. 1 **(d-e)** are attributed to the presence of AL in the electrospinning mixture (**Table S3**).

We now turn to investigate the structural characteristics of ASB1173K, AN, and AN-ASB calcined at 1173 K with XRD. From the results in Fig. 2**(a)**, it is clear that at 1173 K, the γ-Al_2O_3 phase is mainly formed. In Fig. 2**(b)**, we also examine the ASB nanofibers over two new temperatures, i.e., 873 and 1023 K, to corroborate the presence of the γ-Al_2O_3 found at 1173 K in Fig. 2**(a)**. ASB thermally treated at 873 K and 1023 K do not completely transform into the γ-Al_2O_3 crystallographic phase. The formation of an amorphous Al_2O_3 is encountered at 873 K, whereas peak-broadening in XRD has been found more pronounced at 1023 K, indicating a semicrystalline phase [15,108–110]. With this structural analysis, we can identify the temperature range for either amorphous and semicrystalline ASB ANFs, and crystalline γ-Al_2O_3 nanofibers for the ASB precursor. In Fig. 2**(a)** and Fig. 2**(b)**, AL is used as a reference and matched with the ICDD 29–1486 card showing peaks located at 2Θ = 22°, 35°, 39°, 42°, 48°, 63.3°, 69°, which corresponds to (111), (220), (311), (222), (400), (511), and (440) crystal planes from γ-Al_2O_3. From the XRD results, it is fair to say

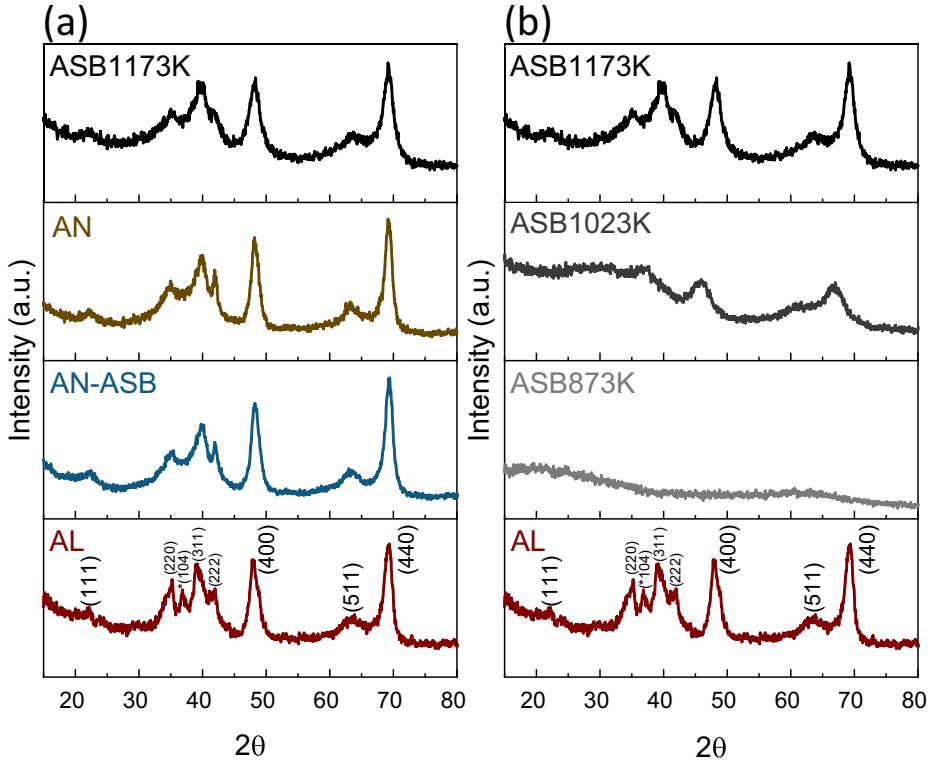

Fig. 2. XRD diffraction patterns of (a) ANFs obtained at 1173 K with various precursors (AN, AN-ASB) and (b) ASB ANFs annealed at 1173, 1023, and 873 K. AL is used for comparison.

that the ANFs in Fig. 2**(a)** is composed of γ-Al_2O_3 phase. It should be noted that for AL reference, another peak appears at 36.8° label with (104) crystal plane, which matches the ICDD 42–1468 card data and therefore corresponds to α-Al_2O_3.

To estimate the acid site distribution per unit volume, we introduce first the results from the textural analysis performed with BET for samples ASB1173K, AN, AN-ASB, and thermally treated ASB at 873 K (ASB873K), and 1023 K (ASB1023K) in Tables 1 and 2. The highest surface area is obtained for ASB873K and ASB1023K with 234 and 200 m^2/g, respectively, followed by ASB1173K with 180 m^2/g. Other formulations like AN and AN-ASB remain below the 77 m^2/g. Compared to commercial γ-Al_2O_3, ASB1173K has a higher surface area than AL but not ALS. The effect can be attributed to sintering or phase transformation for AL,[31] making ASB of value for chemical reactions where γ-Al_2O_3 is required [42]. These findings are significant because it shows that the electrospun ASB precursor can considerably increase the surface area, even higher than commercial γ-Al_2O_3, like AL (114.5 m^2/g) and other ANFs reported in the literature (**Table S1**). Additional evidence showing that the ASB precursor increases the surface area is presented in Table 2. In this case, the ASB1173K nanofibers are compared with drop-casted ASB annealed at 1173 K (hereafter ASB1173K-DC). ASB1173K-DC results in γ-Al_2O_3 but lacks a nanofiber-like structure (**Figure S3**). Surface area measures evidence that the ASB1173K nanofibers retain a higher surface area than ASB1173K-DC in Table 2. The BET results are also in agreement with the total surface area found for ASB1173K (158 m^2/g) and AL (115 m^2/g) measured with mercury (Hg) intrusion. Interestingly, the mean pore diameter for Hg intrusion has been found higher for ASB1173K (ca. 4 μm) than AL (ca. 150 nm). Therefore, it is fair to say that macropores are formed thanks to the non-woven fiber structure of ASB1173K (Fig. 1**(a)**). AL does not count with such structural characteristics, as displayed in **Figure S3**. To this end, the textural properties of the intertwined fibrous network for sample ASB1073K after pressing (3 t/cm^2) (named ASB1023K*) is also assessed in Table 2 to corroborate if changes in the ANFs structure might change the surface area as measured with BET. From the results, it is observed that pressing does not change the textural properties of ASB1073K. Similarities characteristics are expected for the other ANFs in Tables 1 and 2.

Among the ANFs from Tables 1 and 2, it is clear that ASB873K, ASB1023K, and ASB1173K ANFs have the highest specific surface area, even one of the highest reported for nanofibers (Table S1). An in-depth analysis using the BET isotherms from Fig. 3 is assessed to generate insights into the pore type and pore size distribution in ASB ANFs. For this study, ASB is contrasted with γ-Al_2O_3 nanofibers types (AN and AN-ASB), ASB873K, ASB1023K, and commercial γ-Al_2O_3 (AL and ALS). Fig. 3 shows two different sets of adsorption–desorption isotherms. First, pretreated ANFs at 1173 K, i.e., ASB1173K, AN, and AN-ASB in Fig. 3**(a)**. Second, ASB ANFs, i.e., ASB873K, ASB1023K, and ASB1173K in Fig. 3**(c)**, which figure aim to generate insights on the effect of temperature in ASB. Fig. 3**(a,c)** showed hysteresis loops in the multilayer step associated with capillary condensation. Fig. 3**(a)** shows that the isotherm of sample ASB1173 K and ALS are of type IV for meso-

Table 1
Fiber diameter, surface area, and total acidity of γ-Al_2O_3 fibers obtained at 1173 K using different precursors.

Samples annealed at 1173 K	Surface area (m^2/g)	Total acidity (μmol/g)	Total acidity (μmol/m^2)
ASB1173K	180.8	134.3	0.7
AN	63.7	29.7	0.5
AN-ASB	53.3	24.2	0.45
AL	114.5	105.0	0.9
ALS	217.6	212.2	1.0

Table 2
Fiber diameter, surface area, total acidity, and pore size of Al_2O_3 fibers obtained at 873, 1023, and 1173 K using ASB as the precursor. *ASB1023K pressed using 3 t/cm^2.

Sample	Surface area (m^2/g)	Pore size (nm)	Total acidity (μmol/g)	Total acidity (μmol/m^2)
ASB873K	234.5	6.7	141.3	0.6
ASB1023K	200.5	6.4	139.6	0.7
ASB1023K*	198.2	6.7	–	–
ASB1173K	180.8	7.4	134.3	0.7
ASB1173K-DC	100.3	7.5	–	–

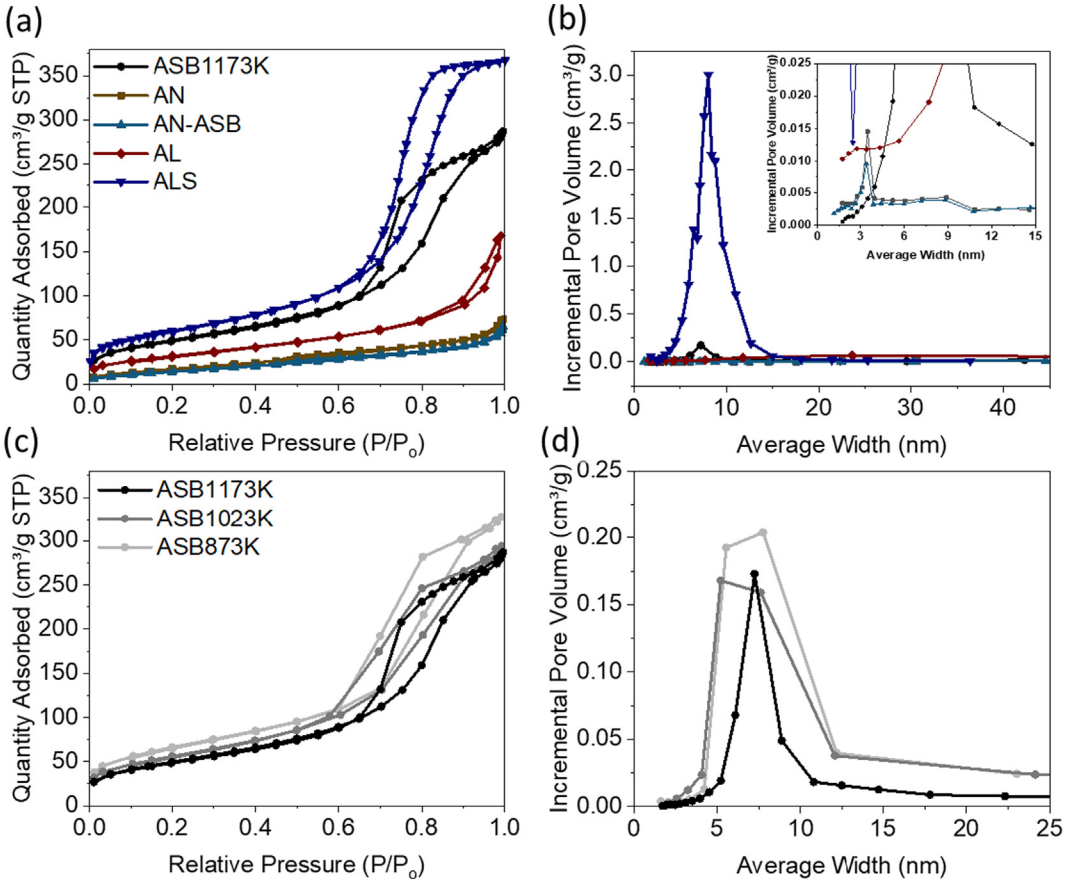

Fig. 3. Adsorption-desorption isotherms and pore size distribution for (a, b) ASB1173K, AN, AN-ASB, AN-ASB-AL ANFs obtained at 1173 K. (c, d) ASB873K, ASB1023K, and ASB1173K. AL and ALS are included for comparison.

pores with H2 hysteresis[111]. In the same figure, the samples AN and AN-ASB and AL showed type II isotherms with H3 hysteresis shape, suggesting slit-shaped pores of non-rigid aggregates of plate-like particles [112,113]. The pore size distribution curves in Fig. 3**(b)** corroborate wider pore bodies for most of the γ-Al_2O_3 nanofibers, excepting ASB that shows a narrow distribution between 7 and 8 nm very much comparable to ALS with 8 nm. It is clear that ASB ANFs have lower incremental pore volume than ALS Fig. 3**(b)** but with the advantage of macropores formation (Fig. 1**(a)**). With such characteristics on hand, the ASB ANFs can be cataloged as a material that combines mesoporosity [10,28,114–117] and microporosity in one.

Results for ASB873K and ASB1023K in Fig. 3**(c)** show great similitude to ASB1173K, where the adsorption–desorption isotherms reveal the type IV with H2 behavior. Differences in the hysteresis loop between ASB873K, ASB1023K, ASB1173K could be attributed to the pore broader bottleneck present at lower temperatures in Fig. 3**(d)**. Similar porosity is maintained for ASB1023K* in Table 2 after compression without compromising the surface area. As temperature increases to 1173 K, narrow pores are observed. From the ANFs, ASB has a narrower pore size distribution with the highest amount of mesopores.

We investigated the porosity formed throughout the ASB ANFs with STEM to support our different temperature experiments from Fig. 3**(c)**. The results are presented in Fig. 4. STEM images in Fig. 4**(a-c)** for ASB873K, ASB1023K, and ASB1173K are recorded in dark field mode. Samples in the row below (Fig. 4**(d-f)**) follow the same order as in Fig. 4**(a-c)**. The bright-field image in Fig. 4**(d)** corresponds to sample ASB873K and reveals a pronounced contrast, where pores throughout the ANFs are seen (yellow arrows). These results confirm that the annealing temperature decreases porosity, particularly when comparing STEM images Fig. 4**(a, d)** with Fig. 4**(b, c)**. The reduction in porosity in Fig. 4**(c)** can be attributed to sintering effects [28]. Furthermore, SEM images for ASB1023K in Fig. 4**(e-f)** help to corroborate surface roughness (dashed ellipses), which is seen in the form of wrinkles found in Fig. 1. It should be noted that all ANFs in Fig. 4 have been subjected to sonication before analysis, and thus, it is expected to observe broken ANFs. To this end, the purity of ASB ANFs is determined by analyzing the chemical surface composition of ASB873K and ASB1173K with

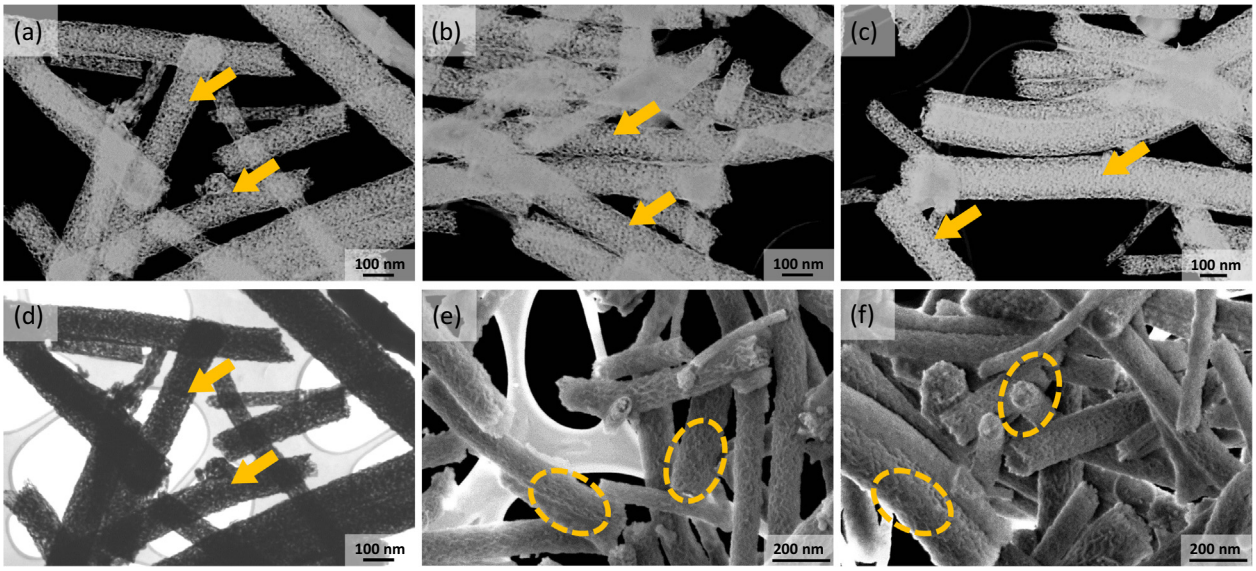

Fig. 4. STEM images for ASB873K, ASB1023K, and ASB1173K ANFs.

XPS. XPS ensures that the produced ASB aluminas between 873 K and 1173 K do not contain residues that might affect the alumina nature (e.g., acid nature). In this case, a possible contaminant is nitrogen species due to PVP. The general survey of the samples revealed only the presence of aluminum and oxygen (**Figure S4**).

3.2. The nature of acidity sites in γ-Al_2O_3 and Al_2O_3 nanofibers

Py is an appropriate probe molecule to study the nature of BAS (protonic acidity) and LAS surface acid sites (aprotic acidity) [42,118]. ASB ANFs have been analyzed with Py adsorption since ASB ANFs showed desirable textural properties in Tables 1 and 2. Commercial AL and ALS are also used for comparison during Py-FTIR experiments. Fig. 5**(a)** shows the FTIR spectra of Py adsorbed on ASB873K, ASB1023K, ASB1173K, AL, and ALS at 303 K. All the samples show bands at 1446, 1577, and 1614 cm^{-1} attributed to Py adsorbed on LAS. The LAS of alumina are produced partly by uncoordinated Al^{3+} and by cation vacancies exposed on the surface [119]. The band around 1594 cm^{-1} is assigned to hydrogen-bonded pyridine [120]. As other authors report,[121] this band completely disappears after heating at 373 K (**Figure S5**). The signal at 1491 cm^{-1} is attributed to Py adsorbed on both Lewis and BAS. However, in our alumina, the contribution to the BAS band is only given by LAS. The absence of the signal at 1540 cm^{-1} of the protonated Py (PyH^+) suggests that BAS are not present in the γ-Al_2O_3[20] nor amorphous and semicrystalline nanofibers. In other words, the OH is not strong enough to protonate the Py[122]. The effect of Py adsorption on the OH group bands is used to characterize further and identify the acid groups. In this case, the OH can be perturbed by the direct hydrogen-bonded pyridine (1594 cm^{-1}) and via hydrogen bonding of the Py ring (adsorbed on LAS) next to an OH adjacent group [120]. Fig. 5**(b)** shows the difference spectra in the high-frequency region recorded at 303 K after Py adsorption. The variation in the OH bands is clear by the negative bands at around 3850 and 3670 cm^{-1}. The hydrogen bonding is evidenced by the positive broad bands around 3500–3400 cm^{-1}. These results further indicate that the Py is adsorbed on LAS and hydrogen-bonded to the surface. For comparison, the IR spectra in the high-frequency region in the absence of Py adsorption at 723 K are presented in **Figure S6**. The results reveal the presence of chemisorbed water in γ-Al_2O_3.

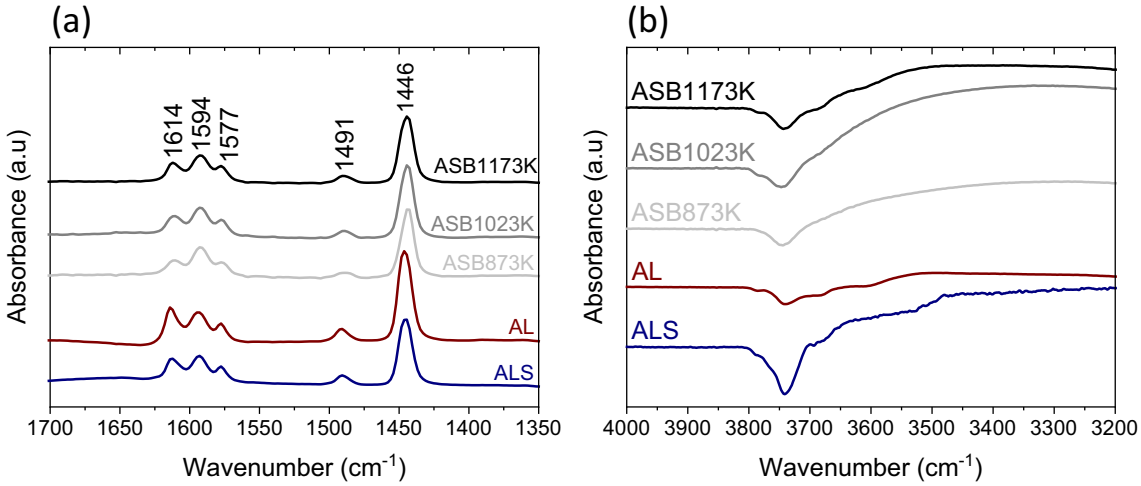

Fig. 5. (a) FTIR spectra after Py adsorption and (b) FTIR high-frequency region spectra after Py adsorption on ASB873K, ASB1023K, ASB1173K, AL, and ALS at 303 K.

To this end, it is important to summarize previous results from Fig. 3, Fig. 4, and Fig. 5. The results reveal two main effects dominating in ASB873K, ASB1023K, ASB1173K. First, the mesoporous character of the ASB nanofibers (Fig. 3), which formation can be correlated to a condensation reaction [86]. PVP (main nanofiber component) used as a template might also introduce mesopore formation in the nanofibers after removal. Small pores can be also be found in Fig. 4 for ASB873K, ASB1023K, ASB1173K. As the temperature increases for ASB873K, ASB1023K, ASB1173K, more dense ANFs are found. AFNs in Fig. 4 suggests a reduction in surface area, as shown in Table 2. Regardless of the ASB ANF type, the nature of the acid sites prevails to be prominently LAS, as shown in Fig. 5. Similar acid sites have been found for AL and ALS in Fig. 5.

3.3. TPD-NH_3 of γ-Al_2O_3 and Al_2O_3 nanofibers

TPD is used to determine the total acidic sites using NH_3 as a probe molecule. In Fig. 6, the NH_3-TPD profiles are presented for ASB1173K, ASB1023K, ASB873K ANFs, and AL. The number of acid sites for ASB ANFs and commercial γ-Al_2O_3 is presented in Table 1 and Table 2. In these tables, the highest content of acid sites has been estimated for ALS, followed by ASB873K, ASB1023K, ASB1173K, AL, AN, and AN-ASB. For the γ-Al_2O_3, the acidity decreases as follows ALS(212.2 μmol/g) > ASB1173K(134 μmol/g) > AL(105 μmol/g) > AN(29.7 μmol/g) >AN-ASB(24.2 μmol/g). Most

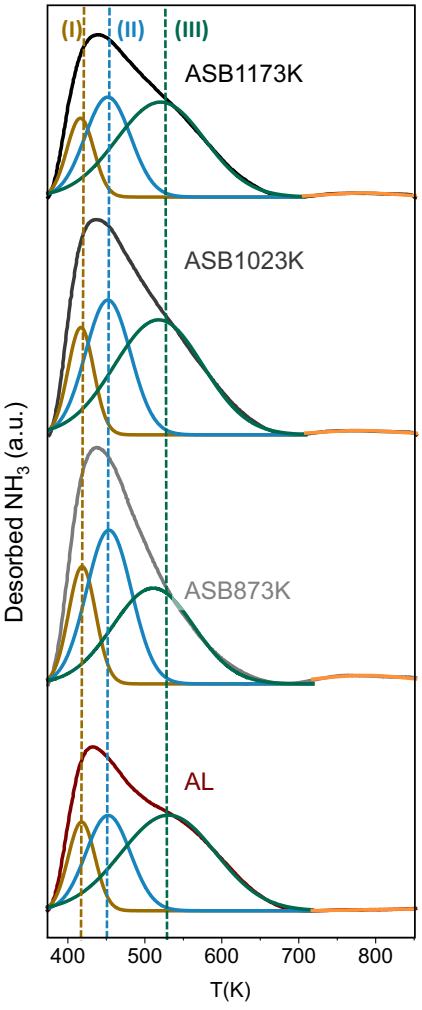

Fig. 6. NH_3-TPD profiles of ASB ANFs obtained at 873, 1023, and 1173 K. AL is used as a control.

of the ANFs show a relatively low amount of acidic sites, except ASB. From these results, the acidity found for the thermally treated ASB ANFs can be directly dependent on the temperature and crystallinity of the formed Al_2O_3 and not on other impurities (**Figure S4**). It has been shown that acidity decreases by increasing the crystallinity of Al_2O_3 [98]. Following the same analogy, the decreased acidity of ASB ANFs can be generated by the loss of defects present in the structure due to crystallinity change from amorphous to γ phase. Therefore, it is reasonable to find a higher content of acid sites for amorphous, semicrystalline Al_2O_3 nanofibers than γ-Al_2O_3 nanofibers.

From the NH_3-TPD results, it is clear that ASB has the highest acid site content among the ANFs. The nature of the acid sites can be attributed to LAS by Pyridine analysis.(Fig. 5**(a)**). With NH_3-TPD information, we can estimate the acid site distribution per unit volume of the ANFs (Table 2). The ASB ANFs remain the highest reported in the literature (**Table S1**), with a total acidity of 0.7 μmol/m^2. The other ANFs fall below 0.7 μmol/m^2. Compared to commercial catalysts, the total acidity for ASB1173K seems to be close to AL (0.9 μmol/m^2) and ALS (1 μmol/m^2). The results are quite interesting because ASB ANFs combine most of the desired characteristics of an acid catalyst but have additional structural dimensions in the form of non-woven nanofibers, a feature that is very much appreciated in catalysis [123].

3.3.1. Acid site strength in γ-Al_2O_3 and Al_2O_3 nanofibers

We then proceed to understand the acid strength distribution with NH_3-TPD. The NH_3-TPD results have been analyzed using a Gaussian distribution function. The reason for selecting a Gaussian function is because it is well accepted to provide more reliable and consistent desorption energy data for alumina [124]. In particular, NH_3-TPD for γ-Al_2O_3 can be described as a linear combination of three Gaussian curves [125]. Therefore, we proceed to deconvolute all measured NH_3-TPD profiles in three Gaussian peaks. Each of these peaks were assigned over three regions corresponding to weak (373–433 K), medium (433–533 K), and strong acid sites (533–773 K). Weak (I), medium (II), and strong (III) acid sites are colored in brown, light blue, and green in Fig. 6. The Py-FTIR and NH_3-TPD results suggest that weak LAS contributes to the TPD peak[126] located between 373 and 433 K since hydrogen bonded desorb at temperatures below 373 K [127,128,129]. On the other hand, medium and strong LAS might be expected for an NH_3-TPD temperature range between 433 and 773 K (Fig. 6**(a)** and **Figure S5**) [127–130]. It should be mentioned that acidity has tremendous repercussions during chemical transformation. Some examples in the field of heterogeneous catalysis are listed in **Table S2**. Understanding how molecular adsorbates, such as NH_3, interact with γ-Al_2O_3 can help generate insights into acid sites mediated reaction mechanisms in γ-Al_2O_3 [20].

3.3.2. NH_3 desorption kinetics

We can further generate valuable insights into the overall desorption kinetics with DFT on a γ-Al_2O_3(1 1 0) model system with one chemisorbed H_2O molecule [96,97,98]. On this model system, the presence of chemisorbed and adsorbed H_2O is studied first (**Figure S1**) to verify if H_2O is eliminated during the temperature pretreatment at 673 K or higher temperatures. After such treatment, we can still expect some chemisorbed water on nanofibers and commercial γ-Al_2O_3, also confirmed with FTIR in **Figure S6**. Therefore, we consider the bare γ-Al_2O_3(1 1 0)-model system with one chemisorbed water as representative of the state of γ-Al_2O_3 before NH_3 adsorption. Moreover, 4 different exposed Al-sites are on the surface (Fig. 7), labeled as empty sites *1, *2, *3, and *4. This model system thus contains various relevant adsorption sites that can be representative for the γ-Al_2O_3 ANFs. The Al-site *1 is coordinated to 3 oxygen atoms, and *2, is coordinated to 4 oxygen

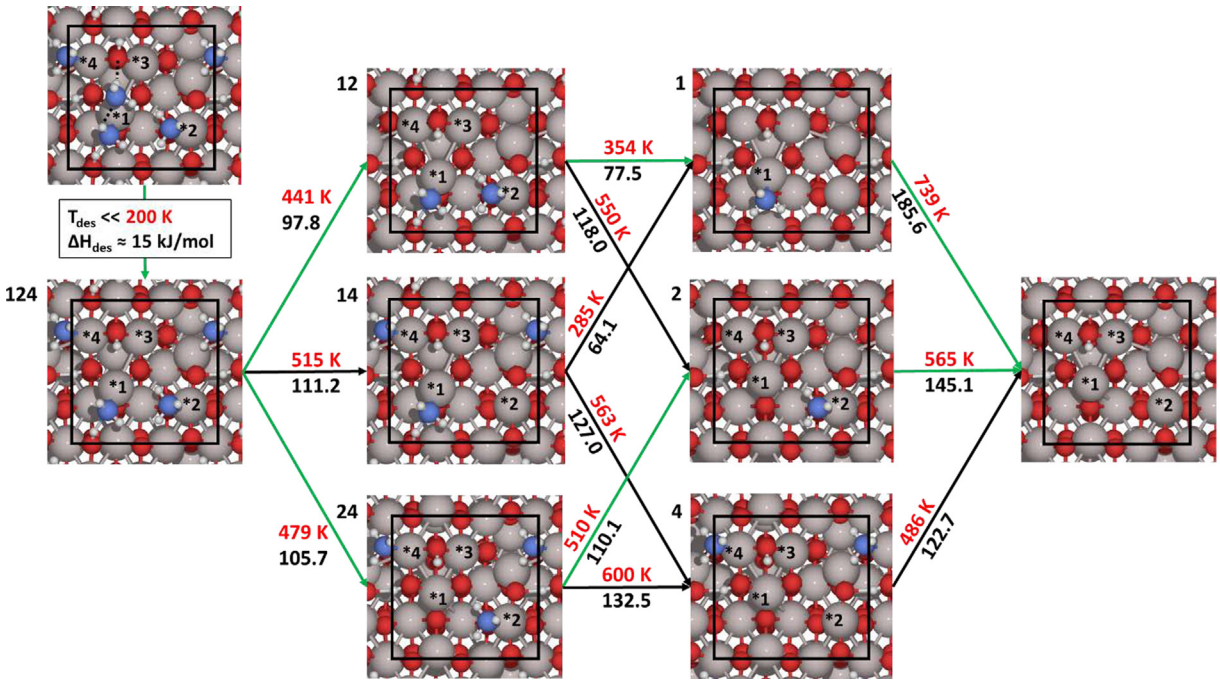

Fig. 7. Schematic reaction pathway of plausible desorption pathways starting from a γ-Al_2O_3 [110] model system with chemisorbed water. The different NH_3 adsorption sites with their respective desorption temperature T_{des}, (K, red) and ΔH_{des} (kJ/mol, black). Atomic color codes: Al (gray), O (red), N (blue), H (white), the periodic repeating unit (black rectangle). (For interpretation of the references to color in this figure legend, the reader is referred to the web version of this article.)

atoms, while *3 and *4 are coordinated to 5 oxygen atoms. In fact, *3 and *4 could be considered active sites of great similitude. It should be noted that the Al-site coordination to oxygen atoms might vary for the ASB-derived γ-Al_2O_3 nanofibers or commercial catalysts. In other words, each γ-Al_2O_3 will have a different population and distribution of adsorption sites. Therefore, the current computational study can provide understandings into the NH_3 adsorption and desorption on different Al-sites.

The expected adsorption configuration for NH_3 is given in Fig. 7. The configuration with adsorbed NH_3 group is labeled according to the sites NH_3 occupies. In the following, we refer to the possible adsorption configurations with a number code (left upper side of each panel, e.g., **124**). In **124**, the adsorption configuration is with 3 NH_3 molecules. Most of the contributions during NH_3 desorption might be expected for LAS and BAS. However, when studying various BAS at high NH_3 coverage (Fig. 7), the typical adsorption enthalpies observed were between −10 and −15 kJ/mol, which would correspond with desorption temperatures below 200 K at an NH_3 partial pressure of 100 Pa. Experimentally, only LAS and hydrogenbond Py have been observed on γ-Al_2O_3 as identified with Py-FTIR and in agreement with our model, NH_3 adsorbed by hydrogenbond is expected to desorb below the 373 K, if any. For the analysis, the NH_3 partial pressure during TPD is estimated at 100 Pa for the chemisorbed water model system in Fig. 7. However, it should be noted that a lower NH_3 partial pressure results in lower desorption temperatures, which you can expect for non-chemisorbed water. In supporting information, computational results are also presented for a γ-Al_2O_3(1 1 0)-model system without chemisorbed water (**Figs S7, S8,** and **S9**, **Table S4**).

The stepwise desorption of NH_3 can be determined, as shown in Fig. 7. However, if we consider the different sites at low loading, the most strongly adsorbing Al-site is *1, which has an adsorption enthalpy (ΔH_{ads}) of ca. −185.6 kJ/mol and thus a desorption enthalpy (ΔH_{des}) of 185.6 kJ/mol (i.e., -ΔH_{ads} = ΔH_{des}). This high NH_3 adsorption energy can be understood since *1 is the Al-site with the lowest oxygen coordination number ($CN_{Al\text{-}*1}$ = 3). The other considered Al-sites in the γ-Al_2O_3(1 1 0)-model system (*2, *3, and *4) have a higher oxygen coordination number (CN = 4 or 5), which results in less strongly adsorbed NH_3 molecules with ΔH_{des} below 145 kJ/mol. Adsorption of an NH_3 molecule over *4 results in an ΔH_{des} = 122.7 kJ/mol, and for *2, we find ΔH_{des} = 14 5.1 kJ/mol. The ΔH_{des} is estimated using the mobile adsorbate approach for physisorbed NH_3, while the immobile adsorbate approach is taken for chemisorbed NH_3 (only for *1).

To gain insight into the overall desorption kinetics process of TPD on γ-Al_2O_3 (1 1 0), we require an understanding of the subsequent NH_3 desorption. This implies that after desorption in Fig. 7, there is an additional relocation of NH_3 until exhaustion from the γ-Al_2O_3 (1 1 0) surface. Therefore, the thermodynamic stability of NH_3 over γ-Al_2O_3(1 1 0) at different ammonia partial pressures (p_{NH_3}) and temperature is presented in **Figure S8**. In this figure, it is possible to optimize the γ-Al_2O_3 (1 1 0) surface with two additional NH_3 adsorbates. However, desorption of the first two NH_3 molecules happens easily, with average ΔH_{des} near 0 kJ/mol [129]. Hence, model systems with fewer NH_3 molecules are considered to be more suitable to study subsequent NH_3 desorption. In this approach, NH_3 is loaded over Al-sites, as shown in Fig. 7. From the analysis, we derive the free energy difference for various temperatures and an NH_3 partial pressure of 1 mbar in Table 3. The most likely desorption pathway takes place by initial removal of hydrogen-bonded NH_3, i.e. **124** ↔ **124** + NH_3, followed by NH_3 on LAS; **124** ↔ **12** + NH_3 ↔ **1** + $2NH_3$ ↔ **empty** + $3NH_3$ and **124** ↔ **24** + NH_3 ↔ **2** + $2NH_3$ ↔ **empty** + $3NH_3$. If for the last desorption step from the most stable physisorbed NH_3, i.e. **1** ↔ **empty** + NH_3, a lower NH_3 pressure of 0.25 mbar is assumed, the desorption temperature lowers from 739 K (1 mbar) to 703 K (0.25 mbar) irrespective of the presence of chemisorbed water. However, there is another desorption pathway very likely, suppose that the chemisorbed NH_3 at ***1** is desorbed first, requiring only a desorption enthalpy of 105.7 kJ/mol and this step becomes already exergonic at 479 K. Therefore, it is clear that at high NH_3 coverage of our model system, even chemisorbed NH_3 can desorb first. This

Table 3
Most likely, desorption pathways of NH_3 starting from **124** in Fig. 7 for mobile adsorbates at p_{NH_3} = 100 Pa.

Reaction	T_{des} (K)	ΔH_{des} (kJ/mol)	ΔG_{des} (kJ/mol)					
			300 K	400 K	500 K	600 K	700 K	800 K
124 ↔ 12 + NH_3	441	97.8	31.0	8.9	−13.1	−34.9	−56.5	−80.0
124 ↔ 24 + NH_3	479	105.7	39.0	17.1	−4.7	−26.2	−47.5	−68.5
124 ↔ 14 + NH_3	515	111.2	46.2	24.6	3.1	−18.1	−39.2	−60.1
12 ↔ 1 + NH_3	354	77.5	11.7	−10.1	−31.7	−53.1	−74.2	−95.1
12 ↔ 2 + NH_3	550	118.0	53.2	31.7	10.4	−10.6	−31.3	−51.9
14 ↔ 1 + NH_3	300	64.1	−3.4	−25.8	−48.0	−69.9	−91.5	−112.9
14 ↔ 4 + NH_3	563	127.0	59.0	36.4	13.9	−8.3	−30.2	−52.0
24 ↔ 2 + NH_3	510	110.1	45.0	23.4	2.0	−19.3	−40.4	−61.3
24 ↔ 4 + NH_3	600	132.5	66.0	43.8	21.7	−0.2	−22.0	−43.6
1 ↔ empty + NH_3	739	173.6	101.5	77.7	54.3	31.3	8.6	−13.8
2 ↔ empty + NH_3	565	145.1	67.3	41.5	16.1	−8.9	−33.7	−58.1
4 ↔ empty + NH_3	486	122.7	46.4	21.2	−3.6	−28.0	−52.1	−75.8

would then yield structure **24**, from which the NH_3 group at position ***4** desorbs at 510 K (p_{NH_3} = 100 Pa), which can be followed by NH_3 desorption from ***2** at 565 K. While the desorption temperature for the reaction sequence **124** ↔ **24** + NH_3 ↔ **2** + $2NH_3$ ↔ **empty** + $3NH_3$, are thus respectively 479, 510 and 565 K at an NH_3 partial pressure of 100 Pa. Lowering the NH_3 partial pressure to 10 Pa, results in lowered desorption temperatures by about 40 K, i.e. 440, 468, and 525 K. The latter 3 temperatures agree well with the temperature ranges that were used to fit Gaussians to the experimental TPD data, i.e., 373–433 K, 433–533 K, and 533–773 K (Fig. 6). However, it should be noted that compared with the experiment data, we would need to know the distribution of adsorption sites, especially the % of *1 sites. These threefold coordinated Al-sites can have the highest desorption at low NH_3 coverage enthalpies, which ultimately result in the highest desorption temperatures.

In general, the extracted experimental desorption kinetics typically varies between γ-Al_2O_3 and might contain another site distribution present in our atomistic model. Nevertheless, the model may be compared with the experimental conditions of the NH_3-TPD, by assuming that at the begging of the TPD analysis, all the different acid sites of the alumina are fully covered (coverage (θ) of NH_3 on alumina is θ = 1), which is in agreement with the protocol followed by the theoretical calculations by determining one NH_3 molecule per active site.

Once the desorption temperature range for the acid site range is defined, a kinetic order analysis of multisite NH_3-TPD[131] is employed. This model is based on the linearization of the integral function of the Polanyi-Wigner equation. It is worth mentioning that, in our case, the empirical desorption energy (E_d) values correspond to the apparent desorption energy due to the exclusion of the readsorption processes in the mathematical model, which is highly possible at low heating rates. Moreover, a pre-exponential factor of 10^{11} s^{-1} is assumed (value reported for γ- Al_2O_3) [132]. By following the regression procedure outlined for different desorption reaction orders in **Table S5** at a coverage (θ) = 1 (explained above in the text), we found that the NH_3-TPD of ASB1173K, AL, and ALS follow zero- and first-order desorption kinetics [131]. The approach uses the experimentally recorded NH_3-TPD from Fig. 6 for γ-Al_2O_3 only. The desorption energy for each of the acid types assigned can be estimated using the proposed empirical approach [131]. For the approach, the apparent desorption energy (E_d) for ASB1173K, AL and ALS can be correlated to ΔH_{ads} by the equation [q_{ad} = -ΔH^0_{ads} = E_d + 1/2 RT], [133] leading to an estimation of the desorption enthalpy, i.e. ΔH_{ads} = -ΔH_{des}. The averaged E_d results from the temperature range for weak, medium, and strong acid sites.

As it is seen from **Table S5,** different desorption orders are observed for the different acid types. The difference may be attributed to different desorption kinetics due to the different distribution of acid type in γ-Al_2O_3. A first-order desorption kinetic model is most appropriate for weak and medium sites based on the highest R^2 value (**Table S5**) and literature [132–136]. To illustrate our kinetic order calculation, the linear regression of the function ln(θ_i,θ_i-Δθ) vs. inverse temperature (1/K) is plotted in **Figure S10** [133]. With such an approach, the calculated E_d interval for the weak (374–433 K) and medium (433–532 K) acid site is ∼ [-96, −106] kJ/mol and [-106, −132] kJ/mol, respectively. Even with the variation in acid site distribution, these E_d results are comparable to **Table S4** and show increased desorption energies at higher temperatures. Then the, zero-order desorption kinetic model resulted in a better fit for the mathematical modeling of strong acid sites (533–773 K) with the highest desorption energies and temperatures (**Table S5** and **Figure S10**). The zero-order desorption kinetic can be attributed to NH_3 readsorption, which significantly lowers the kinetic order close to zero [129]. The derived apparent desorption energy interval for strong acid sites is [-115, −171] kJ/mol (**Table S5**). For comparison, the estimated values for the apparent desorption energy interval for n = 0 and n = 1 are presented in **Table S6**.

Finally, from the desorption kinetic study, we can derive the following conclusions: (**i**) the R^2 results in the supporting information support the kinetic desorption order (n) = 0 or 1. (**ii**) The simulated desorption kinetics process of TPD is derived from 4 different desorption steps. We can compare the final desorption energy for an empty surface with these desorption steps, assuming a surface coverage close to zero. For low coverage, the most stable adsorbed/physisorbed NH_3 is *1 with an estimated ΔH_{des} of 173.6 kJ/mol for physisorbed NH_3 at 739 K for the mobile adsorbate approach, while for the standard immobile adsorbate approach, this would be a ΔH_{des} of 176.1 kJ/mol at 862 K. Assuming in the mathematical model for desorption a reaction order n = 0, a calculated ΔH_{des} of around 176 kJ/mol is obtained at around 800 K; which lies actually in between the mobile and immobile adsorbate approach [90]. There is thus a close similarity between our mathematical model and the ab initio calculations.

The results for ASB-derived γ-Al_2O_3 nanofibers have comparable kinetic desorption properties to AL and ALS. The advantages of nanofibers are foreseen microporosity, acidity, and relatively high surface area among fibrous materials (Table 1). ASB nanofiber properties can be of great interest in catalysis. Several methods have been used to synthesize ANFs, including sol–gel and solvothermal, amongst others (Table 1). We aim to position electrospinning as a synthesis method of catalytic supports, where the fiber's macroporosity can facilitate reactants and product diffusion during a catalytic reaction. Additionally, the small diameter of the nanofibers makes short diffusion pores, ensuring the absence of

diffusional limitations. Electrospinning and any other of their configurations can provide the tools for developing a structured catalyst where acidity and porosity can be controlled. The ultimate alumina material will be useful for specific chemical reactions (**Table S3**).

4. Conclusions

γ-Al_2O_3 nanofibers with high acidity and surface area have been prepared using electrospinning from different Al_2O_3 precursors. The surface area for these non-woven nanofiber specimens, measured with BET, indicates the presence of pores in the range of 4.5–10 nm. The synthesized γ-Al_2O_3 nanofibers have a tunable surface area in the range of 180–235 m^2/g and acidity of 0.6–0.7 μmol/m^2 with ASB Al_2O_3/γ-Al_2O_3 the best among the other ANFs. For ASB γ-Al_2O_3 nanofibers, macroporosity is evidenced (ca. 4 μm). Furthermore, ASB γ-Al_2O_3 nanofibers reveal LAS prominently. DFT calculations provided fundamental insight into the adsorption/desorption thermodynamics during NH_3 adsorption/desorption and clearly showed increasing desorption energies with increasing temperature. Furthermore, comparing empirical mathematical modeling and experiments helps create a desorption map for weak, medium, and strong acid sites. This work forms a basis for further utilization of electrospun alumina nanofibers in the field of heterogeneous catalysis.

Declaration of Competing Interest

The authors declare that they have no known competing financial interests or personal relationships that could have appeared to influence the work reported in this paper.

Acknowledgments

The authors thank Stephan Bartling (Leibniz Institute for Catalysis), Regina Lange and Ingo Barke (University of Rostock, Institute of Physics), Frank Morssinkhof (Membrane Science & Technology Cluster, University of Twente), and Mark Smithers (MESA + Institute, University of Twente) for their support. M.V. wishes to acknowledge the Irish Centre for High-End Computing (ICHEC) for the provision of computational facilities and support. The research leading to the results in this report has received funding from the European Research Council (ERC) under the European Union's Horizon 2020 research and innovation program (Grant agreement No. 742004).

Appendix A. Supplementary material

Supplementary data to this article can be found online at https://doi.org/10.1016/j.jcat.2021.11.019.

References

[1] M. Zabeti, W.M.A. Wan Daud, M.K. Aroua, Activity of solid catalysts for biodiesel production: A review, Fuel Process. Technol. 90 (6) (2009) 770–777, https://doi.org/10.1016/j.fuproc.2009.03.010.
[2] M. Zabeti, W.M.A.W. Daud, M.K. Aroua, Optimization of the activity of CaO/Al2O3 catalyst for biodiesel production using response surface methodology, Appl. Catal. A Gen. 366 (1) (2009) 154–159, https://doi.org/10.1016/j.apcata.2009.06.047.
[3] T.S. Nguyen, M. Zabeti, L. Lefferts, G. Brem, K. Seshan, Conversion of lignocellulosic biomass to green fuel oil over sodium based catalysts, Bioresour. Technol. 142 (2013) 353–360, https://doi.org/10.1016/j.biortech.2013.05.023.
[4] Z. Zhang, R.W. Hicks, T.R. Pauly, T.J. Pinnavaia, Mesostructured forms of γ-Al2O3, J. Am. Chem. Soc. 124 (8) (2002) 1592–1593, https://doi.org/10.1021/ja016974o.
[5] M.A. Mellmer, C. Sanpitakseree, B. Demir, K. Ma, W.A. Elliott, P. Bai, R.L. Johnson, T.W. Walker, B.H. Shanks, R.M. Rioux, M. Neurock, J.A. Dumesic, Effects of chloride ions in acid-catalyzed biomass dehydration reactions in polar aprotic solvents, Nat. Commun. 10 (2019) 1–10, https://doi.org/10.1038/s41467-019-09090-4.
[6] R. Alamillo, M. Tucker, M. Chia, Y. Pagán-Torres, J. Dumesic, The selective hydrogenation of biomass-derived 5-hydroxymethylfurfural using heterogeneous catalysts, Green Chem. 14 (2012) 1413–1419, https://doi.org/10.1039/c2gc35039d.
[7] X. Xu, H. Zhang, Y. Tong, Y. Sun, X. Fang, J. Xu, X. Wang, Tuning Ni3+ quantity of NiO via doping of cations with varied valence states: The key role of Ni3+ on the reactivity, Appl. Surf. Sci. 550 (2021) 149316, https://doi.org/10.1016/j.apsusc.2021.149316.
[8] L.C. Buelens, V. V. Galvita, H. Poelman, C. Detavernier, G.B. Marin, Super-dry reforming of methane intensifies CO2 utilization via le Chatelier's principle, Science (80-.). 354 (2016) 449–452. https://doi.org/10.1126/science.aah7161.
[9] D. Li, Y.i. Li, X. Liu, Y. Guo, C.-W. Pao, J.-L. Chen, Y. Hu, Y. Wang, NiAl2O4 Spinel Supported Pt Catalyst: High Performance and Origin in Aqueous-Phase Reforming of Methanol, ACS Catal. 9 (10) (2019) 9671–9682, https://doi.org/10.1021/acscatal.9b02243.
[10] C. Italiano, J. Llorca, L. Pino, M. Ferraro, V. Antonucci, A. Vita, CO and CO2 methanation over Ni catalysts supported on CeO2, Al2O3 and Y2O3 oxides, Appl. Catal. B Environ. 264 (2020) 118494, https://doi.org/10.1016/j.apcatb.2019.118494.
[11] H. Jeong, O. Kwon, B.-S. Kim, J. Bae, S. Shin, H.-E. Kim, J. Kim, H. Lee, Highly durable metal ensemble catalysts with full dispersion for automotive applications beyond single-atom catalysts, Nat. Catal. 3 (4) (2020) 368–375, https://doi.org/10.1038/s41929-020-0427-z.
[12] J. Ihli, R.R. Jacob, M. Holler, M. Guizar-Sicairos, A. Diaz, J.C. Da Silva, D. Ferreira Sanchez, F. Krumeich, D. Grolimund, M. Taddei, W.C. Cheng, Y. Shu, A. Menzel, J.A. Van Bokhoven, A three-dimensional view of structural changes caused by deactivation of fluid catalytic cracking catalysts, Nat. Commun. 8 (2017) 1–10. https://doi.org/10.1038/s41467-017-00789-w.
[13] Jimmie L Williams, Monolith structures, materials, properties and uses, Catal. Today. 69 (1-4) (2001) 3–9, https://doi.org/10.1016/S0920-5861(01)00348-0.
[14] I. Levin, D. Brandon, Metastable alumina polymorphs: Crystal structures and transition sequences, J. Am. Ceram. Soc. 81 (1998) 1995–2012, https://doi.org/10.1111/j.1151-2916.1998.tb02581.x.
[15] G. Busca, The surface of transitional aluminas : A critical review, Catal. Today. 226 (2014) 2–13, https://doi.org/10.1016/j.cattod.2013.08.003.
[16] B. Kasprzyk-hordern, Chemistry of alumina , reactions in aqueous solution and its application in water treatment, 110 (2004) 19–48. https://doi.org/10.1016/j.cis.2004.02.002.
[17] J. Ruiz, C. Jimenez-Sanchidrian, Heterogeneous Catalysis in the Meerwein-Ponndorf-Verley Reduction of Carbonyl Compounds, Curr. Org. Chem. 11 (2007) 1113–1125, https://doi.org/10.2174/138527207781662500.
[18] Z. Wang, T. Li, Y. Jiang, O. Lafon, Z. Liu, J. Trébosc, A. Baiker, J.P. Amoureux, J. Huang, Acidity enhancement through synergy of penta- and tetra-coordinated aluminum species in amorphous silica networks, Nat. Commun. 11 (2020) 1–9, https://doi.org/10.1038/s41467-019-13907-7.
[19] Ken Motokura, Mizuki Tada, Yasuhiro Iwasawa, Heterogeneous organic base-catalyzed reactions enhanced by acid supports, J. Am. Chem. Soc. 129 (31) (2007) 9540–9541, https://doi.org/10.1021/ja0704333.
[20] Bhausaheb Dhokale, Arturo Susarrey-Arce, Anna Pekkari, August Runemark, Kasper Moth-Poulsen, Christoph Langhammer, Hanna Härelind, Michael Busch, Matthias Vandichel, Henrik Sundén, Microwave-heated γ-Alumina Applied to the Reduction of Aldehydes to Alcohols, ChemCatChem 12 (24) (2020) 6344–6355, https://doi.org/10.1002/cctc.v12.2410.1002/cctc.202001284.
[21] D. Guillaume, S. Gautier, I. Despujol, F. Alario, P. Beccat, Characterization of acid sites on γ-alumina and chlorinated γ-alumina by31P NMR of adsorbed trimethylphosphine, Catal. Letters. 43 (1997) 213–218, https://doi.org/10.1023/A:1018955025955.
[22] W. Lueangchaichaweng, B. Singh, D. Mandelli, W.A. Carvalho, S. Fiorilli, P.P. Pescarmona, High surface area, nanostructured boehmite and alumina catalysts: Synthesis and application in the sustainable epoxidation of alkenes, Appl. Catal. A Gen. 571 (2019) 180–187, https://doi.org/10.1016/j.apcata.2018.12.017.
[23] Theodore F. Baumann, Alexander E. Gash, Sarah C. Chinn, April M. Sawvel, Robert S. Maxwell, Joe H. Satcher, Synthesis of high-surface-area alumina aerogels without the use of alkoxide precursors, Chem. Mater. 17 (2) (2005) 395–401, https://doi.org/10.1021/cm048800m.
[24] M. Trueba, S.P. Trasatti, γ -Alumina as a Support for Catalysts, A Review of Fundamental Aspects (2005) 3393–3403, https://doi.org/10.1002/ejic.200500348.
[25] Lingli Peng, Xiangyu Xu, Zhi Lv, Jiaqing Song, Mingyuan He, Qian Wang, Lijun Yan, Yang Li, Zhaofei Li, Thermal and morphological study of Al2O3 nanofibers derived from boehmite precursor, in, J. Therm. Anal. Calorim. 110 (2) (2012) 749–754, https://doi.org/10.1007/s10973-011-1962-2.
[26] W. Deng, M.W. Toepke, B.H. Shanks, Surfactant-assisted synthesis of alumina with hierarchical nanopores, Adv. Funct. Mater. 13 (2003) 61–65, https://doi.org/10.1002/adfm.200390007.
[27] J.S. Lee, H.S. Kim, N.K. Park, T.J. Lee, M. Kang, Low temperature synthesis of α-alumina from aluminum hydroxide hydrothermally synthesized using [Al(C2O4)x(OH)y] complexes, Chem. Eng. J. 230 (2013) 351–360, https://doi.org/10.1016/j.cej.2013.06.099.

[28] Y. Wang, W. Li, X. Jiao, D. Chen, Electrospinning preparation and adsorption properties of mesoporous alumina fibers, J. Mater. Chem. A. 1 (2013) 10720–10726, https://doi.org/10.1039/c3ta10955k.
[29] Arturo Susarrey-Arce, Miguel Angel Hernández-Espinosa, Fernando Rojas-González, Christopher Reed, Vitalii Petranovskii, Angel Licea, Inception and Trapping of ZnO Nanoparticles within Desilicated Mordenite and ZSM-5 Zeolites, Part. Part. Syst. Charact. 27 (3-4) (2010) 100–111, https://doi.org/10.1002/ppsc.201000027.
[30] S. Lowell, J.E. Shields, M.A. Thomas, M. Thommes, Characterisation of Porous Solids and Powders (2004), https://doi.org/10.1007/978-1-4020-2303-3.
[31] P. Euzen, P. Raybaud, X. Krokidis, H. Toulhoat, J.-L. Le Loarer, J.-P. Jolivet, C. Froidefond, 4.7.2, Alumina, Handb. Porous Solids. 3 (2002).
[32] Carlos Márquez-Alvarez, Naděžda Žilková, Joaquín Pérez-Pariente, Jiří Čejka, Synthesis, characterization and catalytic applications of organized mesoporous aluminas, Catal. Rev. - Sci. Eng. 50 (2) (2008) 222–286, https://doi.org/10.1080/01614940701804042.
[33] Stacy M. Morris, Pasquale F. Fulvio, Mietek Jaroniec, Ordered mesoporous alumina-supported metal oxides, J. Am. Chem. Soc. 130 (45) (2008) 15210–15216, https://doi.org/10.1021/ja806429q.
[34] Quan Yuan, An-Xiang Yin, Chen Luo, Ling-Dong Sun, Ya-Wen Zhang, Wen-Tao Duan, Hai-Chao Liu, Chun-Hua Yan, Facile synthesis for ordered mesoporous γ-aluminas with high thermal stability, J. Am. Chem. Soc. 130 (11) (2008) 3465–3472, https://doi.org/10.1021/ja0764308.
[35] Sonia Carre, Benoit Tapin, Ngi Suor Gnep, Renaud Revel, Patrick Magnoux, Model reactions as probe of the acid-base properties of aluminas: Nature and strength of active sites, Correlation with physicochemical characterization, Appl. Catal. A Gen. 372 (1) (2010) 26–33, https://doi.org/10.1016/j.apcata.2009.10.005.
[36] Watcharop Chaikittisilp, Hyung-Ju Kim, Christopher W. Jones, Mesoporous alumina-supported amines as potential steam-stable adsorbents for capturing CO2 from simulated flue gas and ambient air, Energy Fuels 25 (11) (2011) 5528–5537, https://doi.org/10.1021/ef201224v.
[37] F. Rascón, R. Wischert, C. Copéret, Molecular nature of support effects in single-site heterogeneous catalysts: Silica vs. alumina, Chem. Sci. 2 (2011) 1449–1456, https://doi.org/10.1039/c1sc00073j.
[38] Weiquan Cai, Jiaguo Yu, Chokkalingam Anand, Ajayan Vinu, Mietek Jaroniec, Facile synthesis of ordered mesoporous alumina and alumina-supported metal oxides with tailored adsorption and framework properties, Chem. Mater. 23 (5) (2011) 1147–1157, https://doi.org/10.1021/cm102512v.
[39] Yogesh C. Sharma, Bhaskar Singh, John Korstad, Latest developments on application of heterogenous basic catalysts for an efficient and eco friendly synthesis of biodiesel: A review, Fuel 90 (4) (2011) 1309–1324, https://doi.org/10.1016/j.fuel.2010.10.015.
[40] W. Cai, L. Tan, J. Yu, M. Jaroniec, X. Liu, B. Cheng, F. Verpoort, Synthesis of amino-functionalized mesoporous alumina with enhanced affinity towards Cr(VI) and CO2, Chem. Eng. J. 239 (2014) 207–215, https://doi.org/10.1016/j.cej.2013.11.011.
[41] Z. Xu, J. Yu, M. Jaroniec, Efficient catalytic removal of formaldehyde at room temperature using AlOOH nanoflakes with deposited Pt, Appl. Catal. B Environ. 163 (2015) 306–312, https://doi.org/10.1016/j.apcatb.2014.08.017.
[42] H. Knözinger, P. Ratnasamy, Catalytic Aluminas: Surface Models and Characterization of Surface Sites, Catal. Rev. 17 (1) (1978) 31–70, https://doi.org/10.1080/03602457808080878.
[43] C.Vinod Chandran, Christine E.A. Kirschhock, Sambhu Radhakrishnan, Francis Taulelle, Johan A. Martens, Eric Breynaert, Alumina: Discriminative analysis using 3D correlation of solid-state NMR parameters, Chem. Soc. Rev. 48 (1) (2019) 134–156, https://doi.org/10.1039/C8CS00321A.
[44] A. Quindimil, U. De-La-Torre, B. Pereda-Ayo, A. Davó-Quiñonero, E. Bailón-García, D. Lozano-Castelló, J.A. González-Marcos, A. Bueno-López, J.R. González-Velasco, Effect of metal loading on the CO2 methanation: A comparison between alumina supported Ni and Ru catalysts, Catal. Today. 356 (2020) 419–432, https://doi.org/10.1016/j.cattod.2019.06.027.
[45] G. Busca, Silica-alumina catalytic materials: A critical review, Catal. Today. 357 (2020) 621–629, https://doi.org/10.1016/j.cattod.2019.05.011.
[46] M. Iwai, T. Kikuchi, R.O. Suzuki, Self-ordered nanospike porous alumina fabricated under a new regime by an anodizing process in alkaline media, Sci. Rep. 11 (2021) 1–8, https://doi.org/10.1038/s41598-021-86696-z.
[47] Nassim Bouchoul, Houcine Touati, Elodie Fourré, Jean-Marc Clacens, Isabelle Batonneau-Gener, Catherine Batiot-Dupeyrat, Plasma-catalysis coupling for CH4 and CO2 conversion over mesoporous macroporous Al2O3: Influence of the physico-chemical properties, Appl. Catal. B Environ. 295 (2021) 120262, https://doi.org/10.1016/j.apcatb.2021.120262.
[48] Naicai Xu, Zhong Liu, Shaoju Bian, Yaping Dong, Wu Li, Template-free synthesis of mesoporous γ-alumina with tunable structural properties, Ceram. Int. 42 (3) (2016) 4072–4079, https://doi.org/10.1016/j.ceramint.2015.11.079.
[49] Stephen A. Bagshaw, Thomas J. Pinnavaia, Mesoporous Alumina Molecular Sieves, Angew. Chemie (International Ed. English) 35 (10) (1996) 1102–1105, https://doi.org/10.1002/(ISSN)1521-377310.1002/anie.v35:1010.1002/anie.199611021.
[50] Claudio Morterra, Giuliana Magnacca, A case study: Surface chemistry and surface structure of catalytic aluminas, as studied by vibrational spectroscopy of adsorbed species, Catal. Today. 27 (3-4) (1996) 497–532, https://doi.org/10.1016/0920-5861(95)00163-8.
[51] J.M. McHale, A. Auroux, A.J. Perrotta, A. Navrotsky, Surface energies and thermodynamic phase stability in nanocrystalline aluminas, Science (80-.). 277 (1997) 788–789. https://doi.org/10.1126/science.277.5327.788.
[52] Morris D. Argyle, Kaidong Chen, Alexis T. Bell, Enrique Iglesia, Effect of catalyst structure on oxidative dehydrogenation of ethane and propane on alumina-supported vanadia, J. Catal. 208 (1) (2002) 139–149, https://doi.org/10.1006/jcat.2002.3570.
[53] X. Bokhimi, J. Sánchez-Valente, F. Pedraza, Crystallization of sol-gel boehmite via hydrothermal annealing, J. Solid State Chem. 166 (1) (2002) 182–190, https://doi.org/10.1006/jssc.2002.9579.
[54] Guohui Li, Linjie Hu, Josephine M. Hill, Comparison of reducibility and stability of alumina-supported Ni catalysts prepared by impregnation and co-precipitation, Appl. Catal. A Gen. 301 (1) (2006) 16–24, https://doi.org/10.1016/j.apcata.2005.11.013.
[55] M. Digne, P. Sautet, P. Raybaud, P. Euzen, H. Toulhoat, Use of DFT to achieve a rational understanding of acid-basic properties of γ-alumina surfaces, J. Catal. 226 (2004) 54–68, https://doi.org/10.1016/j.jcat.2004.04.020.
[56] A. Lind, Ø. Vistad, M.F. Sunding, K.A. Andreassen, J.H. Cavka, C.A. Grande, Multi-purpose structured catalysts designed and manufactured by 3D printing, Mater. Des. 187 (2020) 1–8, https://doi.org/10.1016/j.matdes.2019.108377.
[57] Cesar Parra-Cabrera, Clement Achille, Simon Kuhn, Rob Ameloot, 3D printing in chemical engineering and catalytic technology: Structured catalysts, mixers and reactors, Chem. Soc. Rev. 47 (1) (2018) 209–230, https://doi.org/10.1039/C7CS00631D.
[58] Simge Danaci, Lidia Protasova, Vesna Middelkoop, Nachiketa Ray, Michel Jouve, Alain Bengaouer, Philippe Marty, Scaling up of 3D printed and Ni/Al2O3 coated reactors for CO2 methanation, React, Chem. Eng. 4 (7) (2019) 1318–1330, https://doi.org/10.1039/C9RE00092E.
[59] D. Han, X. Li, L. Zhang, Y. Wang, Z. Yan, S. Liu, Hierarchically ordered meso/macroporous γ-alumina for enhanced hydrodesulfurization performance, Microporous Mesoporous Mater. 158 (2012) 1–6, https://doi.org/10.1016/j.micromeso.2012.03.022.
[60] R. Takahashi, S. Sato, T. Sodesawa, K. Arai, M. Yabuki, Effect of diffusion in catalytic dehydration of alcohol over silica-alumina with continuous macropores, J. Catal. 229 (1) (2005) 24–29, https://doi.org/10.1016/j.jcat.2004.10.010.
[61] S. Cavaliere, S. Subianto, I. Savych, D.J. Jones, J. Rozière, Electrospinning: Designed architectures for energy conversion and storage devices, Energy Environ. Sci. 4 (2011) 4761–4785, https://doi.org/10.1039/c1ee02201f.
[62] H.U. Shin, A. Abutaleb, D. Lolla, G.G. Chase, Effect of calcination temperature on NO-CO decomposition by Pd catalyst nanoparticles supported on alumina nanofibers, Fibers. 5 (2017) 1–14, https://doi.org/10.3390/fib5020022.
[63] Yan Wang, Wei Li, Yuguo Xia, Xiuling Jiao, Dairong Chen, Electrospun flexible self-standing γ-alumina fibrous membranes and their potential as high-efficiency fine particulate filtration media, J. Mater. Chem. A. 2 (36) (2014) 15124–15131, https://doi.org/10.1039/C4TA01770F.
[64] Biyun Li, Huihua Yuan, Pengfei Yang, Bingcheng Yi, Yanzhong Zhang, Fabrication of the composite nanofibers of NiO/γ-Al2O3 for potential application in photocatalysis, Ceram. Int. 42 (15) (2016) 17405–17409, https://doi.org/10.1016/j.ceramint.2016.08.040.
[65] Chen Liang, Wensheng Liu, Qiang Liu, Yangrui Gao, Jijin Liu, Juan Wang, Shuwei Yao, Yunzhu Ma, The formation of core-sheath structure and its effects on thermal decomposition and crystallization of alumina fibers, Ceram. Int. 47 (4) (2021) 5145–5155, https://doi.org/10.1016/j.ceramint.2020.10.092.
[66] Xiangyu Meng, Wanlin Xu, Zhihui Li, Jianhui Yang, Jingwu Zhao, Xixi Zou, Yueming Sun, Yunqian Dai, Coupling of Hierarchical Al 2 O 3 / TiO 2 Nanofibers into 3D Photothermal Aerogels Toward Simultaneous Water Evaporation and Purification, Adv. Fiber Mater. 2 (2) (2020) 93–104, https://doi.org/10.1007/s42765-020-00029-9.
[67] Hongqin Dai, Jian Gong, Hakyong Kim, Doukrae Lee, A novel method for preparing ultra-fine alumina-borate oxide fibres via an electrospinning technique, Nanotechnology. 13 (5) (2002) 674–677, https://doi.org/10.1088/0957-4484/13/5/327.
[68] Andrei Stanishevsky, W. Anthony Brayer, Pavel Pokorny, Tomáš Kalous, David Lukáš, Nanofibrous alumina structures fabricated using high-yield alternating current electrospinning, Ceram. Int. 42 (15) (2016) 17154–17161, https://doi.org/10.1016/j.ceramint.2016.08.003.
[69] Xiaolei Song, Ying Song, Juan Wang, Qiang Liu, Zhenxin Duan, Insights into the pore-forming effect of polyvinyl butyral (PVB) as the polymer template to synthesize mesoporous alumina nanofibers via electrospinning, Ceram. Int. 46 (7) (2020) 9952–9956, https://doi.org/10.1016/j.ceramint.2019.12.107.
[70] Jingyi Shen, Zehua Li, Yi-nan Wu, Bingru Zhang, Fengting Li, Dendrimer-based preparation of mesoporous alumina nanofibers by electrospinning and their application in dye adsorption, Chem. Eng. J. 264 (2015) 48–55, https://doi.org/10.1016/j.cej.2014.11.069.
[71] Dayong Wu, Gang Wang, Weihua Liang, Jianhua Cao, The electrospun mesoporous Al2O3 and mesoporous Au–Al2O3 nanofiber catalyst, J. Porous Mater. 23 (5) (2016) 1373–1379, https://doi.org/10.1007/s10934-016-0196-x.
[72] Veronika Medvecká, Dušan Kováčik, Monika Stupavská, Tomáš Roch, Alexander Kromka, Radek Fajgar, Anna Zahoranová, Mirko Černák, Preparation and characterization of alumina submicron fibers by plasma assisted calcination, Ceram. Int. 46 (14) (2020) 22774–22780, https://doi.org/10.1016/j.ceramint.2020.06.044.

[73] Lei Li, Xiaolian Liu, Gang Wang, Yalin Liu, Weimin Kang, Nanping Deng, Xupin Zhuang, Xinghai Zhou, Research progress of ultrafine alumina fiber prepared by sol-gel method: A review, Chem. Eng. J. 421 (2021) 127744, https://doi.org/10.1016/j.cej.2020.127744.
[74] Xing-hai Zhou, Wei-min Kang, Wei Xu, Bo-wen Cheng, Flexible hollow CeO2/Al2O3 fibers: Preparation, characterization and dye adsorption efficiency, RSC Adv. 5 (103) (2015) 84535–84542, https://doi.org/10.1039/C5RA14540F.
[75] Shima Valinejad Moghaddam, Mehran Rezaei, Fereshteh Meshkani, Reihaneh Daroughegi, Synthesis of nanocrystalline mesoporous Ni/Al2O3–SiO2 catalysts for CO2 methanation reaction, Int. J. Hydrogen Energy. 43 (41) (2018) 19038–19046, https://doi.org/10.1016/j.ijhydene.2018.08.163.
[76] Xueyuan Tang, Yuxi Yu, Electrospinning preparation and characterization of alumina nanofibers with high aspect ratio, Ceram. Int. 41 (8) (2015) 9232–9238, https://doi.org/10.1016/j.ceramint.2015.04.157.
[77] A. Mahapatra, B.G. Mishra, G. Hota, Synthesis of ultra-fine α-Al2O3 fibers via electrospinning method, Ceram. Int. 37 (7) (2011) 2329–2333, https://doi.org/10.1016/j.ceramint.2011.03.028.
[78] Christoph Weidmann, Kirstin Brezesinski, Christian Suchomski, Kristin Tropp, Natascha Grosser, Jan Haetge, Bernd M. Smarsly, Torsten Brezesinski, Morphology-controlled synthesis of nanocrystalline η-Al 2O 3 thin films, powders, microbeads, and nanofibers with tunable pore sizes from preformed oligomeric oxo-hydroxo building blocks, Chem. Mater. 24 (3) (2012) 486–494, https://doi.org/10.1021/cm202692q.
[79] X. Yang, Æ.C. Shao, Æ.Y. Liu, Fabrication of Cr 2 O 3 / Al 2 O 3 composite nanofibers by electrospinning, (2007) 8470–8472. https://doi.org/10.1007/s10853-007-1769-5.
[80] A.F. Lotus, R.K. Feaver, L.A. Britton, E.T. Bender, D.A. Perhay, N. Stojilovic, R.D. Ramsier, G.G. Chase, Characterization of TiO 2 – Al 2 O 3 composite fibers formed by electrospinning a sol – gel and polymer mixture, 167 (2010) 55–59. https://doi.org/10.1016/j.mseb.2010.01.027.
[81] A.F. Lotus, Y.C. Kang, J.I. Walker, R.D. Ramsier, G.G. Chase, Effect of aluminum oxide doping on the structural , electrical , and optical properties of zinc oxide (AOZO) nanofibers synthesized by electrospinning, 166 (2010) 61–66. https://doi.org/10.1016/j.mseb.2009.10.001.
[82] A.M. Azad, Fabrication of transparent alumina (Al2O3) nanofibers by electrospinning, Mater. Sci. Eng. A. 435–436 (2006) 468–473, https://doi.org/10.1016/j.msea.2006.07.075.
[83] Wanlin Fu, Yunqian Dai, Jerry Pui Ho Li, Zebang Liu, Yong Yang, Yibai Sun, Yiyang Huang, Rongwei Ma, Lan Zhang, Yueming Sun, Unusual Hollow Al2O3 Nanofibers with Loofah-Like Skins: Intriguing Catalyst Supports for Thermal Stabilization of Pt Nanocrystals, ACS Appl. Mater. Interfaces. 9 (25) (2017) 21258–21266, https://doi.org/10.1021/acsami.7b04196.
[84] Mike Tebyetekerwa, Seeram Ramakrishna, What Is Next for Electrospinning?, Matter 2 (2) (2020) 279–283, https://doi.org/10.1016/j.matt.2020.01.004.
[85] Rüdiger Nass, Helmut Schmidt, Synthesis of an alumina coating from chelated aluminium alkoxides, J. Non. Cryst. Solids. 121 (1-3) (1990) 329–333, https://doi.org/10.1016/0022-3093(90)90153-D.
[86] L. Ji, J. Lin, K.L. Tan, H.C. Zeng, Synthesis of high-surface-area alumina using aluminum tri-sec-butoxide-2,4-pentanedione-2-propanol-nitric acid precursors, Chem. Mater. 12 (4) (2000) 931–939, https://doi.org/10.1021/cm990404u.
[87] Long Zhang, Jerry C.C. Chan, Hellmut Eckert, Gundula Helsch, Lars P. Hoyer, Günther H. Frischat, Novel sol-gel synthesis of sodium aluminophosphate glass based on aluminum lactate, Chem. Mater. 15 (14) (2003) 2702–2710, https://doi.org/10.1021/cm030155g.
[88] Saloua Rezgui, Bruce C. Gates, Sol-Gel Synthesis of Alumina in the Presence of Acetic Acid: Distinguishing Gels and Gelatinous Precipitates by NMR Spectroscopy, Chem. Mater. 6 (12) (1994) 2386–2389, https://doi.org/10.1021/cm00048a028.
[89] Hussein Qasim Hussein, Patrick de Wit, Emiel J. Kappert, Nieck E. Benes, Sustainable Route to Inorganic Porous Hollow Fibers with Superior Properties, ACS Sustain, Chem. Eng. 3 (12) (2015) 3454–3460, https://doi.org/10.1021/acssuschemeng.5b01248.
[90] C.A. Léon Y León, New perspectives in mercury porosimetry, Adv. Colloid Interface Sci. 76–77 (1998) 341–372. https://doi.org/10.1016/S0001-8686(98)00052-9.
[91] Silvana R. Matkovic, Marta Bosco, Sebastián E. Collins, Laura E. Briand, Tailored Brønsted and Lewis surface acid sites of the phosphotungstic Wells Dawson heteropoly-acid, Appl. Surf. Sci. 495 (2019) 143565, https://doi.org/10.1016/j.apsusc.2019.143565.
[92] G. Kresse, J. Furthmüller, Efficiency of ab-initio total energy calculations for metals and semiconductors using a plane-wave basis set, Comput. Mater. Sci. 6 (1) (1996) 15–50, https://doi.org/10.1016/0927-0256(96)00008-0.
[93] G. Kresse, J. Furthmüller, Efficient iterative schemes for *ab initio* total-energy calculations using a plane-wave basis set, Phys. Rev. B. 54 (16) (1996) 11169–11186, https://doi.org/10.1103/PhysRevB.54.11169.
[94] J. Wellendorff, K.T. Lundgaard, A. Møgelhøj, V. Petzold, D.D. Landis, J.K. Nørskov, T. Bligaard, K.W. Jacobsen, Density functionals for surface science: Exchange-correlation model development with Bayesian error estimation, Phys. Rev. B. 85 (2012), https://doi.org/10.1103/PhysRevB.85.235149 235149.
[95] P.E. Blöchl, Projector augmented-wave method, Phys. Rev. B. 50 (24) (1994) 17953–17979, https://doi.org/10.1103/PhysRevB.50.17953.
[96] Raphael Wischert, Pierre Florian, Christophe Copéret, Dominique Massiot, Philippe Sautet, Visibility of Al Surface Sites of γ-Alumina: A Combined Computational and Experimental Point of View, J. Phys. Chem. C. 118 (28) (2014) 15292–15299, https://doi.org/10.1021/jp503277m.
[97] Simon Klacar, Henrik Grönbeck, H2 dissociation over Ag/Al2O3: The first step in hydrogen assisted selective catalytic reduction of NOx, Catal, Sci. Technol. 3 (1) (2013) 183–190, https://doi.org/10.1039/C2CY20343J.
[98] Raphael Wischert, Christophe Copéret, Françoise Delbecq, Philippe Sautet, Optimal water coverage on alumina: A key to generate lewis acid-base pairs that are reactive towards the C-H bond activation of methane, Angew. Chemie - Int. Ed. 50 (14) (2011) 3202–3205, https://doi.org/10.1002/anie.201006794.
[99] An Ghysels, Toon Verstraelen, Karen Hemelsoet, Michel Waroquier, Veronique Van Speybroeck, TAMkin: A versatile package for vibrational analysis and chemical kinetics, J. Chem. Inf. Model. 50 (9) (2010) 1736–1750, https://doi.org/10.1021/ci100099g.
[100] Mikkel Jørgensen, Henrik Grönbeck, Adsorbate Entropies with Complete Potential Energy Sampling in Microkinetic Modeling, J. Phys. Chem. C. 121 (13) (2017) 7199–7207, https://doi.org/10.1021/acs.jpcc.6b11487.
[101] P. Stoltze, Surface Science as the Basis for the Understanding of the Catalytic Synthesis of Ammonia, Phys. Scr. 36 (5) (1987) 824, https://doi.org/10.1088/0031-8949/36/5/010.
[102] K. Reuter, M. Scheffler, Composition, structure, and stability of RuO2 (110) as a function of oxygen pressure, Phys. Rev. B - Condens. Matter Mater. Phys. 65 (2002) 1–11, https://doi.org/10.1103/PhysRevB.65.035406.
[103] Gustavo Larsen, Raffet Velarde-Ortiz, Kevin Minchow, Antonio Barrero, Ignacio G. Loscertales, A method for making inorganic and hybrid (organic/inorganic) fibers and vesicles with diameters in the submicrometer and micrometer range via sol-gel chemistry and electrically forced liquid jets, J. Am. Chem. Soc. 125 (5) (2003) 1154–1155, https://doi.org/10.1021/ja028983i.
[104] B. Ren, M. Fan, L. Tan, R. Li, D. Song, Q. Liu, J. Wang, B. Zhang, X. Jing, Electrospinning synthesis of porous Al2O3 nanofibers by pluronic P123 triblock copolymer surfactant and properties of uranium (VI)-sorption, Mater. Chem. Phys. 177 (2016) 190–197, https://doi.org/10.1016/j.matchemphys.2016.04.017.
[105] J.H. Kim, S.J. Yoo, D.H. Kwak, H.J. Jung, T.Y. Kim, K.H. Park, J.W. Lee, Characterization and application of electrospun alumina nanofibers, Nanoscale Res. Lett. 9 (2014) 1–6, https://doi.org/10.1186/1556-276X-9-44.
[106] C. Peng, J. Zhang, Z. Xiong, B. Zhao, P. Liu, Fabrication of porous hollow γ-Al2O3 nanofibers by facile electrospinning and its application for water remediation, Microporous Mesoporous Mater. 215 (2015) 133–142, https://doi.org/10.1016/j.micromeso.2015.05.026.
[107] A.P. Vogel, B. Van Dyk, A.M. Saib, GTL using efficient cobalt Fischer-Tropsch catalysts, Catal. Today. 259 (2015) 323–330, https://doi.org/10.1016/j.cattod.2015.06.018.
[108] Louise Samain, Aleksander Jaworski, Mattias Edén, Danielle M. Ladd, Dong-Kyun Seo, F. Javier Garcia-Garcia, Ulrich Häussermann, Structural analysis of highly porous γ-Al2O3, J. Solid State Chem. 217 (2014) 1–8, https://doi.org/10.1016/j.jssc.2014.05.004.
[109] Jitendra Gangwar, Bipin Kumar Gupta, Surya Kant Tripathi, Avanish Kumar Srivastava, Phase dependent thermal and spectroscopic responses of Al2O3 nanostructures with different morphogenesis, Nanoscale. 7 (32) (2015) 13313–13344, https://doi.org/10.1039/C5NR02369F.
[110] P. Souza Santos, H. Souza Santos, S.P. Toledo, Standard transition aluminas. Electron microscopy studies, Mater. Res. 3 (4) (2000) 104–114, https://doi.org/10.1590/S1516-14392000000400003.
[111] K.S.W. Sing, D.H. Everett, R.A.W. Haul, L. Moscou, R.A. Pierotti, J. Rouquerol, T. Siemieniewska, Reporting Physisorption Data for Gas/Solid Systems with Special Reference to the Determination of Surface Area and Porosity, Pure Appl. Chem. 57 (1985) 603–619, https://doi.org/10.1351/pac198557040603.
[112] Muhammad B.I. Chowdhury, Rouhong Sui, Rahima A. Lucky, Paul A. Charpentier, One-pot procedure to synthesize high surface area alumina nanofibers using supercritical carbon dioxide, Langmuir 26 (4) (2010) 2707–2713, https://doi.org/10.1021/la902738y.
[113] H.Y. Zhu, J.D. Riches, J.C. Barry, γ-Alumina nanofibers prepared from aluminum hydrate with poly(ethylene oxide) surfactant, Chem. Mater. 14 (5) (2002) 2086–2093, https://doi.org/10.1021/cm010736a.
[114] Yuan Shi, Kai-xi Jiang, Ting-an Zhang, Jun-hua Guo, Ai-chun Zhao, Clean production of porous-Al(OH)3 from fly ash, J. Hazard. Mater. 393 (2020) 122371, https://doi.org/10.1016/j.jhazmat.2020.122371.
[115] Fatemeh Hosseinzadeh, Hossein Sarpoolaky, Sol-Gel Synthesis of Mesoporous Alumina Considering the Simultaneous Effects of Preparation Parameters by Response Surface Methodology, J. Inorg. Organomet. Polym. Mater. 29 (6) (2019) 1956–1971, https://doi.org/10.1007/s10904-019-01155-7.
[116] Sourav Ghosh, Milan Kanti Naskar, M. Estebanez, Solvothermal conversion of nanofiber to nanorod-like mesoporous γ-Al2O3 powders, and study their adsorption efficiency for Congo red, J. Am. Ceram. Soc. 96 (6) (2013) 1698–1701, https://doi.org/10.1111/jace.12368.
[117] Kenneth S.W. Sing, Ruth T. Williams, Physisorption hysteresis loops and the characterization of nanoporous materials, Adsorpt. Sci. Technol. 22 (10) (2004) 773–782, https://doi.org/10.1260/0263617053499032.
[118] E.P. Parry, An Infrared Study of Pyridi, J. Catal. 2 (1963) 371–379.
[119] Xinsheng Liu, Ralph E. Truitt, DRFT-IR studies of the surface of γ-Alumina, J. Am. Chem. Soc. 119 (41) (1997) 9856–9860, https://doi.org/10.1021/ja971214s.
[120] Xinsheng Liu, DRIFTS study of surface of γ-alumina and its dehydroxylation, J. Phys. Chem. C. 112 (13) (2008) 5066–5073, https://doi.org/10.1021/jp711901s.

[121] G. Crépeau, V. Montouillout, A. Vimont, L. Mariey, T. Cseri, F. Maugé, Nature, structure and strength of the acidic sites of amorphous silica alumina: An IR and NMR study, J. Phys. Chem. B. 110 (2006) 15172–15185, https://doi.org/10.1021/jp062252d.
[122] C.A. EMEIS, ChemInform Abstract: Determination of Integrated Molar Extinction Coefficients for IR Absorption Bands of Pyridine Adsorbed on Solid Acid Catalysts, ChemInform. 24 (38) (1993) no–no, https://doi.org/10.1002/chin.199338056.
[123] N. Wakao, J.M. Smith, Diffusion in catalyst pellets, Chem. Eng. Sci. 17 (11) (1962) 825–834, https://doi.org/10.1016/0009-2509(62)87015-8.
[124] P.J. Barrie, Analysis of temperature programmed desorption (TPD) data for the characterisation of catalysts containing a distribution of adsorption sites, Phys. Chem. Chem. Phys. 10 (2008) 1688–1696, https://doi.org/10.1039/B717430F.
[125] F. Arena, R. Di Chio, G. Trunfio, An experimental assessment of the ammonia temperature programmed desorption method for probing the surface acidic properties of heterogeneous catalysts, Appl. Catal. A Gen. 503 (2015) 227–236, https://doi.org/10.1016/j.apcata.2015.05.035.
[126] M. Tamura, K.I. Shimizu, A. Satsuma, Comprehensive IR study on acid/base properties of metal oxides, Appl. Catal. A Gen. 433–434 (2012) 135–145, https://doi.org/10.1016/j.apcata.2012.05.008.
[127] Xiaoliang Fang, Zhaohui Liu, Ming-Feng Hsieh, Mei Chen, Pengxin Liu, Cheng Chen, Nanfeng Zheng, Hollow mesoporous aluminosilica spheres with perpendicular pore channels as catalytic nanoreactors, ACS Nano 6 (5) (2012) 4434–4444, https://doi.org/10.1021/nn3011703.
[128] A Sakthivel, S.E Dapurkar, N.M Gupta, S.K Kulshreshtha, P Selvam, The influence of aluminium sources on the acidic behaviour as well as on the catalytic activity of mesoporous H-AlMCM-41 molecular sieves, Microporous Mesoporous Mater. 65 (2-3) (2003) 177–187, https://doi.org/10.1016/j.micromeso.2003.08.004.
[129] Hanna Sjövall, Richard J. Blint, Louise Olsson, Detailed Kinetic Modeling of NH 3 and H 2O Adsorption, and NH 3 Oxidation over Cu-ZSM-5, J. Phys. Chem. C. 113 (4) (2009) 1393–1405, https://doi.org/10.1021/jp802449s.
[130] Naoki Toyama, Shinobu Ohki, Masataka Tansho, Tadashi Shimizu, Tetsuo Umegaki, Yoshiyuki Kojima, Influence of aluminum precursors on structure and acidic properties of hollow silica–alumina composite spheres, and their activity for hydrolytic dehydrogenation of ammonia borane, Int. J. Hydrogen Energy. 42 (35) (2017) 22318–22324, https://doi.org/10.1016/j.ijhydene.2017.05.128.
[131] Jian Xu, Junyi Deng, Theoretical Parameter-Free Analysis Model for Temperature-Programmed Desorption (TPD) Spectra, ACS Omega 5 (8) (2020) 4148–4157, https://doi.org/10.1021/acsomega.9b03867.
[132] M.C. Abello, A.P. Velasco, O.F. Gorriz, J.B. Rivarola, Temperature-programmed desorption study of the acidic properties of γ-alumina, Appl. Catal. A, Gen. 129 (1) (1995) 93–100, https://doi.org/10.1016/0926-860X(95)00091-7.
[133] Charles T. Campbell, Jason R.V. Sellers, Enthalpies and entropies of adsorption on well-defined oxide surfaces: Experimental measurements, Chem. Rev. 113 (6) (2013) 4106–4135, https://doi.org/10.1021/cr300329s.
[134] S. Da Ros, E. Barbosa-Coutinho, M. Schwaab, V. Calsavara, N.R.C. Fernandes-Machado, Modeling the effects of calcination conditions on the physical and chemical properties of transition alumina catalysts, Mater. Charact. 80 (2013) 50–61, https://doi.org/10.1016/j.matchar.2013.03.005.
[135] J.P. Joly, M. Khalfallah, D. Bianchi, G.M. Pajonk, Acidity of a microporous amorphous alumina measured by intermittent temperature-programmed desorption of ammonia, Appl. Catal. A, Gen. 98 (1) (1993) 61–70, https://doi.org/10.1016/0926-860X(93)85025-K.
[136] J. Kanervo, T. Keskitalo, R. Slioor, A. Krause, Temperature-programmed desorption as a tool to extract quantitative kinetic or energetic information for porous catalysts, J. Catal. 238 (2) (2006) 382–393, https://doi.org/10.1016/j.jcat.2005.12.026.